Neurobiology of Disease 195 (2024) 106501

Contents lists available at ScienceDirect

Neurobiology of Disease

journal homepage: www.elsevier.com/locate/ynbdi

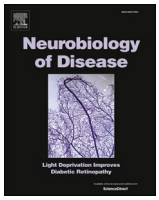

Boosting BDNF in muscle rescues impaired axonal transport in a mouse model of DI-CMTC peripheral neuropathy

Elena R. Rhymes [a,1], Rebecca L. Simkin [a,1], Ji Qu [a], David Villarroel-Campos [a,b], Sunaina Surana [a,b], Yao Tong [c], Ryan Shapiro [c], Robert W. Burgess [d], Xiang-Lei Yang [c], Giampietro Schiavo [a,b], James N. Sleigh [a,b,*]

[a] Department of Neuromuscular Diseases and UCL Queen Square Motor Neuron Disease Centre, Queen Square Institute of Neurology, University College London, London WC1N 3BG, UK
[b] UK Dementia Research Institute at University College London, London WC1N 3BG, UK
[c] Department of Molecular Medicine, The Scripps Research Institute, La Jolla, CA 92037, USA
[d] The Jackson Laboratory, Bar Harbor, ME 04609, USA

ARTICLE INFO

Keywords:
Aminoacyl-tRNA synthetase (ARS)
Charcot-Marie-tooth disease (CMT)
Intravital imaging
Motor neuron
Neuromuscular junction (NMJ)
Neurotrophic factors
Neurotrophins
Peripheral neuropathy
Trk receptors
YARS1

ABSTRACT

Charcot-Marie-Tooth disease (CMT) is a genetic peripheral neuropathy caused by mutations in many functionally diverse genes. The aminoacyl-tRNA synthetase (ARS) enzymes, which transfer amino acids to partner tRNAs for protein synthesis, represent the largest protein family genetically linked to CMT aetiology, suggesting pathomechanistic commonalities. Dominant intermediate CMT type C (DI-CMTC) is caused by *YARS1* mutations driving a toxic gain-of-function in the encoded tyrosyl-tRNA synthetase (TyrRS), which is mediated by exposure of consensus neomorphic surfaces through conformational changes of the mutant protein. In this study, we first showed that human DI-CMTC-causing TyrRS^{E196K} mis-interacts with the extracellular domain of the BDNF receptor TrkB, an aberrant association we have previously characterised for several mutant glycyl-tRNA synthetases linked to CMT type 2D (CMT2D). We then performed temporal neuromuscular assessments of *Yars*^{E196K} mice modelling DI-CMT. We determined that *Yars*^{E196K} homozygotes display a selective, age-dependent impairment in *in vivo* axonal transport of neurotrophin-containing signalling endosomes, phenocopying CMT2D mice. This impairment is replicated by injection of recombinant TyrRS^{E196K}, but not TyrRS^{WT}, into muscles of wild-type mice. Augmenting BDNF in DI-CMTC muscles, through injection of recombinant protein or muscle-specific gene therapy, resulted in complete axonal transport correction. Therefore, this work identifies a non-cell autonomous pathomechanism common to ARS-related neuropathies, and highlights the potential of boosting BDNF levels in muscles as a therapeutic strategy.

1. Introduction

Charcot-Marie-Tooth disease (CMT) is a heritable, genetically diverse form of motor and sensory neuropathy that affects 1 in ≈2500 people (Reilly et al., 2011). Patients display slowly progressive weakness, muscle wasting and sensory dysfunction, which usually manifests in the hands and feet during adolescence, resulting in life-long disability and a significant health and financial burden on society (Schorling et al., 2019). CMT can be categorised into two main subtypes depending on pathogenesis and clinical assessment of nerve conduction

Abbreviations: α-BTX, α-bungarotoxin; AAV, adeno-associated virus; AChR, acetylcholine receptor; ANOVA, analysis of variance; ARS, aminoacyl-tRNA synthetase; BDNF, brain-derived neurotrophic factor; ChAT, choline acetyltransferase; CMT, Charcot-Marie-Tooth Disease; CMT2D, CMT type 2D; DIC, dynein intermediate chain; DI-CMTC, dominant intermediate CMT type C; DRG, dorsal root ganglion/ganglia; ECD, extracellular domain; ETA, epitrochleoanconeous; FDB, flexor digitorum brevis; *GARS1*, GlyRS-encoding gene; GlyRS, glycyl-tRNA synthetase; H_CT, atoxic binding fragment of the tetanus neurotoxin; HDAC6, histone deacetylase 6; ISR, integrated stress response; NCV, nerve conduction velocity; NMJ, neuromuscular junction; NT-3/4/5, neurotrophin-3/4/5; scAAV, self-complementary AAV; Trk, tropomyosin receptor kinase; TyrRS, tyrosyl-tRNA synthetase; *YARS1*, TyrRS-encoding gene.

* Corresponding author at: Department of Neuromuscular Diseases and UCL Queen Square Motor Neuron Disease Centre, Queen Square Institute of Neurology, University College London, London WC1N 3BG, UK.
E-mail address: j.sleigh@ucl.ac.uk (J.N. Sleigh).

[1] Equal contribution

https://doi.org/10.1016/j.nbd.2024.106501
Received 12 March 2024; Received in revised form 4 April 2024; Accepted 4 April 2024
Available online 6 April 2024

velocity (NCV) in the median or ulnar nerve: demyelinating/type 1 CMT (CMT1) and axonal/type 2 CMT (CMT2). CMT1 is caused by the loss of myelinating Schwann cells that ensheath peripheral nerves leading to reduced NCV (<38 m/s), whereas CMT2 is caused by loss of peripheral axons, with little effect on NCV (>45 m/s). Some forms of genetic peripheral neuropathy display clinical features of CMT1 and CMT2, including intermediate NCVs (25–45 m/s), and are thus categorised as intermediate CMT, although this classification can vary (Berciano et al., 2017).

Mutations in >100 genes are currently known to cause CMT, purely motor, or purely sensory inherited neuropathies (Pipis et al., 2019). These genes encode proteins involved in many cellular processes, including mitochondrial biogenesis, axonal transport, protein synthesis and endosomal sorting (Rossor et al., 2013). Many forms of CMT1 are caused by mutations in Schwann cell-critical proteins (*e.g.*, peripheral myelin protein 22 and myelin protein zero), which provides a clear rationale for the selective neuropathology characteristic of CMT. However, the pathomechanisms driving motor and sensory dysfunction in CMT2 are less understood, in part, because the causative genes encode proteins required by many different cells and tissues. Indeed, the gene family linked to the most CMT subtypes encodes aminoacyl-tRNA synthetase (ARS) enzymes, which transfer specific amino acids to cognate tRNAs, and are therefore critical to protein synthesis (Wei et al., 2019).

Seven ARS genes have so far been linked to CMT (*AARS1*, *GARS1*, *HARS1*, *MARS1*, *SARS1*, *WARS1* and *YARS1*) with varying degrees of certainty about pathogenicity (Wei et al., 2019). ARS-related CMT subtypes are all dominantly inherited and display a similar clinical phenotype. Although many ARS mutations affect tRNA aminoacylation, this is not a pre-requisite for disease (Oprescu et al., 2017; Wei et al., 2019; Zhang et al., 2021). Rather, a toxic gain-of-function appears to be the primary driver of neuropathology, at least in the well-studied *GARS1*-linked CMT type 2D (CMT2D) (Grice et al., 2015; Grice et al., 2018; Morelli et al., 2019; Niehues et al., 2015). Indeed, point mutations in *GARS1* have been shown to cause a conformational opening of the encoded glycyl-tRNA synthetase (GlyRS), exposing consensus regions, which are normally buried in the wild-type enzyme, to the protein exterior (He et al., 2015; He et al., 2011). These neomorphic surfaces enable aberrant protein-protein interactions with several intra- and extra-cellular binding partners, including neuropilin-1 (He et al., 2015), tropomyosin receptor kinase (Trk) receptors (Sleigh et al., 2017a) and histone deacetylase 6 (HDAC6) (Mo et al., 2018). Moreover, mutant GlyRS exhibits altered $tRNA^{Gly}$ binding and release, hindering dissociation and causing protein synthesis defects linked to activation of the integrated stress response (ISR) (Spaulding et al., 2021; Zuko et al., 2021).

Neurotrophins are a family of secreted trophic factors that preferentially bind to neuronally-expressed Trk receptors (nerve growth factor to TrkA, brain-derived neurotrophic factor (BDNF) and neurotrophin-4/5 (NT-4/5) to TrkB and neurotrophin-3 (NT-3) to TrkC), enabling local and long-range signalling critical to nerve cell homeostasis (Chao, 2003). We have demonstrated that several different forms of human mutant GlyRS aberrantly associate with the extracellular domains (ECDs) of neurotrophin receptors, whereas $GlyRS^{WT}$ does not (Sleigh et al., 2017a; Sleigh et al., 2023). Further, we recently determined that this mis-interaction between mutant GlyRS and TrkB perturbs axonal transport of neurotrophin-containing signalling endosomes *in vivo*, and that treatment of CMT2D muscles with the TrkB ligand BDNF, but not NT-4, is able to fully rescue the transport disruption (Sleigh et al., 2023). GlyRS is secreted from many different cell types, including neurons and muscle cells, and circulates freely in healthy mouse and human blood (Grice et al., 2015; He et al., 2015), underpinning the significance of this mis-interaction *in vivo*.

Heterozygous point mutations in tyrosyl-tRNA synthetase (TyrRS)-encoding *YARS1* cause demyelinating and axonal neuropathy symptoms that result in a diagnosis of dominant intermediate CMT type C (DI-CMTC) (Jordanova et al., 2006). Patients display mild to moderate disease severity with intermediate NCVs and predominant motor *versus* sensory involvement, which tends to be milder in females (Thomas et al., 2016). DI-CMTC is unlikely to result from haploinsufficiency, since a 50% reduction in *Yars* mRNA produces no overt phenotype in mice (Hines et al., 2022). Additionally, children with severe, multi-system syndromes caused by biallelic *YARS1* loss-of-function mutations display no clear peripheral neuropathy (Nowaczyk et al., 2017; Tracewska-Siemiatkowska et al., 2017), arguing against a loss of *YARS1* function underlying DI-CMTC.

Similar to GlyRS, several different CMT mutations in *YARS1* result in an alternative stable conformation of TyrRS (Blocquel et al., 2017), which enhances its binding affinity for the transcriptional regulators TRIM28 and HDAC1 (Bervoets et al., 2019), as well as F-actin (Ermanoska et al., 2023). Moreover, a *Drosophila* model of DI-CMTC, in which mutant *YARS1* is overexpressed, displays a similar pattern of neuropathology and mRNA translation impairment in motor and sensory neurons to that caused by mutant *GARS1* (Niehues et al., 2015). Furthermore, a new mouse model of DI-CMTC, which carries the E196K mutation in the catalytic domain of TyrRS ($Yars^{E196K}$; see below), displays an activation of the ISR in α motor neurons similar to that identified in CMT2D mice, albeit to a lesser extent (Spaulding et al., 2021). It therefore appears that *GARS1*- and *YARS1*-related neuropathies share key features, suggesting that common gain-of-function mechanism(s) may mediate neuropathology driven by mutations in the ARS-encoding genes.

To better understand DI-CMTC and provide the first mammalian model of the disease, the Burgess Laboratory engineered the Glu196Lys (c.586G > A; p.E196K) patient mutation into exon 5 of the mouse *Yars* gene (also c.586G > A), creating the $Yars^{E196K}$ mouse (Spaulding et al., 2021). The $TyrRS^{E196K}$ mutation has little effect on tyrosine aminoacylation (Froelich and First, 2011; Jordanova et al., 2006), hence $Yars^{E196K}$ mice can be studied as heterozygotes or homozygotes, unlike mouse models for CMT2D (Morelli et al., 2019; Seburn et al., 2006). On a C57BL/6 N background, heterozygous $Yars^{E196K/+}$ mice displayed little to no neuromuscular phenotype. However, homozygous $Yars^{E196K/E196K}$ mice have impaired motor performance in the wire hang test that manifests at 2 months of age and marginally declines by 4 and 7 months (Hines et al., 2022). Additionally, the $Yars^{E196K/E196K}$ mutants exhibited impaired NCVs by 4 months, as well as reduced calibres of motor, but not sensory, axons without any axon loss or myelination defects up to 7 months. Whilst the homozygous mutant mice do not precisely model the human genetics of DI-CMTC, they provide an excellent opportunity to assess whether additional phenotypes are common between DI-CMTC and CMT2D mice, which would be expected if these forms of CMT share underlying pathomechanisms.

In this study, we therefore set out with two main aims: *1*) to determine whether the E196K mutation in *YARS1* triggers a pathological association with the ECD of TrkB similar to that found in CMT2D-linked *GARS1* mutants (Sleigh et al., 2017a; Sleigh et al., 2023); and *2*) to provide further temporal characterisation of neuromuscular phenotypes in $Yars^{E196K/+}$ and $Yars^{E196K/E196K}$ mice to reveal neuropathological similarities between ARS-linked neuropathies in a mammalian setting.

2. Materials and methods

2.1. Animals

Mice were maintained under a 12 h light/dark cycle at a constant room temperature of ≈21 °C with water and food *ad libitum* (Teklad global 18% protein rodent diet, Envigo, 2018C). Cages were enriched with nesting material, plastic/cardboard tubes and wooden chew sticks as standard, and occasionally with cardboard houses. $Yars^{E196K}$ mice originally on a C57BL/6 N background were backcrossed five times onto the C57BL/6 J background and subsequently maintained as heterozygous × wild-type/heterozygous/homozygous breeding pairs. Both males and females were used, details of which are provided in Table S1.

To reduce the number of animals used in this study, multiple assessments were performed on individual mice when possible; for instance, some mice were used for body weight and grip strength testing, prior to euthanising for dissection of muscles and sciatic nerves. Accordingly, a total of 182 mice was used across all experiments. Animals sacrificed for 3, 9 and 15 month time points were 86–99, 265–287 and 450–459 days old, respectively (see Table S1). 8 month-old *Yars*$^{E196K/E196K}$ mice injected with adeno-associated viruses (AAVs) were aged 243–245 days. Post-natal day 1 (P1) was defined as the day after a litter was first found.

2.2. Genotyping

DNA was extracted from ear clips as described previously (Sleigh et al., 2014a) and the following primers were used in a single PCR for genotyping: Yars_F 5′-TGG CTC CAC CCT ATG AGA AC-3′, Yars^{WT}_R 5′-AAA CCA CAC CAA CAG CCT TC-3′ and Yars^{E196K}_R 5'-CCG CGT TAC TTC CTT TTC C-3′. PCR cycling conditions were as follows: 94 °C for 3 min, 35 × [94 °C for 30 s, 60 °C for 35 s, 72 °C for 1 min], 72 °C for 7 min. The wild-type and E196K sequences produce bands of 598 and 660 bp, respectively.

2.3. In vitro pull-down assay

Co-immunoprecipitation experiments using the ECD of human TrkB-Fc (Cys32-His430; R&D Systems, 688-TK) and control human IgG-Fc (110-HG, R&D Systems) were performed in NSC-34 cells (CELLutions Biosystems, CLU140) transfected with plasmids encoding human TyrRS^{WT}-V5, TyrRS^{E196K}-V5 and GlyRS$^{\Delta ETAQ}$-V5, as previously described (Sleigh et al., 2017a; Sleigh et al., 2017b).

2.4. Protein extraction and western blotting

Sciatic nerves and tibialis anterior muscles were dissected from PBS-perfused and non-perfused mice. Proteins were extracted from NSC-34 cells and tissues, and evaluated by western blotting as detailed previously (Sleigh et al., 2023). Primary and secondary antibodies used for western blotting are listed in Table S2 and Table S3, respectively. Densitometry was performed as previously described (Sleigh et al., 2014a) using total protein stained with 0.1% Coomassie Brilliant Blue R-250 (Thermo Fisher, 20,278) as the loading control. Hook1 bands at ≈110 kDa and ≈90 kDa were quantified together in sciatic nerves analyses.

2.5. Immunofluorescence

Dorsal root ganglia (DRG) from spinal levels lumbar 1 (L1) to L5 and cervical 4 (C4) to C8 were dissected (Sleigh et al., 2020e), sectioned, stained and analysed as described elsewhere (Sleigh et al., 2017a). An average of 2022 ± 96 lumbar cells (range 1428-2684) and 365 ± 23 cervical cells (range 279–526) across three to five DRG were assessed in each mouse. The percentages of NF200^{+} and peripherin^{+} cells per mouse were calculated by averaging values from individual DRG. Epitrochleoanconeous (ETA), flexor digitorum brevis (FDB) and hind/forelimb lumbrical muscles were dissected, processed for neuromuscular junction (NMJ) imaging, and analysed as detailed previously (Sleigh et al., 2014b; Sleigh et al., 2014c; Villarroel-Campos et al., 2022). One hundred NMJs per mouse were analysed for assessment of maturation and degenerative phenotypes. Spinal cords were dissected from 4% paraformaldehyde-perfused mice and sectioned at 30 μm; choline acetyltransferase (ChAT)-positive neurons within the L3-L5 anterior horns were counted and their areas measured as previously described (Sleigh et al., 2023). To assess eIF2α activation, spinal cords were processed in parallel; the intensity of phopho-eIF2α staining was determined relative to the intensity of ChAT staining for each motor neuron cell body, as performed elsewhere (Spaulding et al., 2021), before calculating an average per mouse. Primary and secondary antibodies used for immunofluorescence are listed in Table S2 and Table S3, respectively. In addition, AlexaFluor555-conjugated α-bungarotoxin (α-BTX, Life Technologies, B35451) was used at 1:1000 to identify post-synaptic acetylcholine receptors (AChRs). Fluorescent imaging of fixed samples and live nerves (see below) was performed on either an inverted LSM780 or LSM980 laser-scanning microscope (ZEISS).

2.6. In vivo imaging of signalling endosome axonal transport

Live imaging of signalling endosome axonal transport was performed using an atoxic binding fragment of the tetanus neurotoxin (H_CT, residues 875–1315 fused to a cysteine-rich tag and a human influenza haemagglutinin epitope) purified and labelled as formerly described (Gibbs et al., 2016; Restani et al., 2012). *In vivo* imaging and analysis of axonal transport was performed as described previously (Sleigh et al., 2020d; Sleigh et al., 2023; Tosolini et al., 2021), using a pre-warmed environmental chamber set to 38 °C and acquiring images every ≈3 s using a 63× Plan-Apochromat oil immersion objective (ZEISS). For phenotyping at 3, 9 and 15 months, H_CT was injected under isoflurane-induced anaesthesia into the tibialis anterior on one side of the body and the contralateral gastrocnemius; this enabled transport assessment in peripheral nerves supplying distinct hindlimb muscles of the same mouse. To assess the impact of TyrRS on transport, 25 ng/muscle of recombinant human proteins (TyrRS^{WT} or TyrRS^{E196K}, produced as described previously (Ermanoska et al., 2023)) were pre-mixed with H_CT prior to bilateral administration into the tibialis anterior muscles of wild-type mice. The side of injection (tibialis anterior *versus* gastrocnemius, and TyrRS^{WT} *versus* TyrRS^{E196K}) was alternated between mice to eliminate time-under-anaesthesia and right/left biases. Imaging was performed 4–8 h later in both sciatic nerves. By selecting thicker H_CT-positive axons, evaluation of axonal transport in motor axons was prioritised (Sleigh et al., 2020c). To assess trafficking dynamics, 15 endosomes per axon and three to five axons per mouse were manually tracked using the TrackMate plugin on ImageJ (http://rsb.info.nih.gov/ij/) (Tinevez et al., 2017). Endosome reversals were infrequent (<1% of all frame-to-frame movements) and recorded as positive values. Endosome frame-to-frame speeds are presented in frequency histograms; a mean of 393 ± 7 movements (range 279–716) per animal were assessed (in a total of 130 mice across the study).

2.7. Body weight and grip strength testing

Animals were weighed, and all-limb grip strength was assessed using a Grip Strength Meter (Bioseb, GS3). Mice were assessed on two separate days, on which three trials (separated by at least 5 min) were performed. The maximum recorded values from each of the two days were used to calculate a mean grip strength per animal. Relative body weight and grip strength were determined by generating the mean value for wild-type mice of each sex and then calculating individual mouse values as a percentage of the wild-type mean of their respective sex.

2.8. AAV8-tMCK virus production

Self-complementary AAV (scAAV) expression plasmids were created by OXGENE (Oxford, UK); the incorporated sequences of the 745 bp tMCK promoter, 714 bp eGFP and 744 bp human pre-proBDNF are provided elsewhere (Sleigh et al., 2023). pSF-scAAV-tMCK-eGFP and pSF-scAAV-tMCK-BDNF plasmids were packaged into AAV serotype 8 particles by Charles River Laboratories (formerly Vigene Biosciences, Rockville, MD, USA). Viruses were stored at −80 °C in 0.01% (*v*/v) pluronic F68 surfactant in PBS and diluted in sterile PBS for injection.

2.9. Intramuscular injections of BDNF and AAV

To assess the impact of boosting muscle BDNF on endosome axonal transport, bilateral injections into the tibialis anterior muscles of

Yars$^{E196K/E196K}$ mice were performed under isoflurane-induced anaesthesia. Acute treatment was evaluated in 9 month-old mice by premixing and co-administering 5 μg H_CT-555 with 25 ng recombinant human BDNF (Peprotech, 450–02) into one tibialis anterior muscle and 5 μg H_CT-555 with PBS vehicle into the contralateral tibialis anterior, both in a volume of ≈2.5 μl per muscle. For analysing longer term treatment, 10 μl bilateral injections of 2.0×10^{11} vg AAV8-tMCK-eGFP into one tibialis anterior and 2.0×10^{11} vg AAV8-tMCK-BDNF into the contralateral tibialis anterior were performed in 8 month-old mice. 29–30 days post-AAV treatment, *in vivo* axonal transport of signalling endosomes was assessed at 9 months as described above. For these treatments, the side of injection was alternated between mice to avoid biases.

2.10. Statistics

Data were assumed to be normally distributed unless evidence to the contrary were provided by the Kolmogorov-Smirnov test for normality, while equal variance between groups was assumed. The Bonferroni correction was applied to the Kolmogorov-Smirnov tests within each experiment. Normally-distributed data were analysed using unpaired and paired *t*-tests or one-way and two-way analysis of variance (ANOVA) tests followed by Šídák's multiple comparisons test. Non-normally distributed data were analysed using a Mann-Whitney *U* test, Wilcoxon matched-pairs signed rank test or Kruskal-Wallis test followed by Dunn's multiple comparisons test. Sample sizes, which were predetermined using power calculations and previous experience (Sleigh et al., 2014b; Sleigh et al., 2017a; Sleigh et al., 2014c; Sleigh et al., 2020a; Sleigh et al., 2020b; Sleigh et al., 2020c; Sleigh et al., 2023), are reported in figure legends and represent biological replicates (*i.e.*, individual animals). Means ± SEM are plotted for all graphs. All tests were two-sided and an α-level of $P < 0.05$ was used to determine significance. GraphPad Prism 10 software (version 10.1.1) was used for statistical analyses and figure production.

3. Results

3.1. TyrRS^{E196K} mis-interacts with the extracellular domain of TrkB

Our initial aim in this study was to test whether the TyrRS^{E196K} mutant aberrantly interacts with the ECD of TrkB. To do this, we transfected NSC-34 cells with constructs encoding V5-tagged human TyrRS^{WT}, TyrRS^{E196K} or GlyRS$^{\Delta ETAQ}$, with the latter included as a positive control (Sleigh et al., 2023). Cells were subsequently lysed and co-immunoprecipitation experiments performed with the ECD of Fc-tagged TrkB. Western blotting of pull-downs performed in triplicate revealed that TyrRS^{E196K} does indeed mis-associate with TrkB to a higher extent than TyrRS^{WT}, but less than GlyRS$^{\Delta ETAQ}$ (Fig. 1A-B). Importantly for a potential shared pathomechanism with GlyRS, TyrRS is also secreted and is found in blood (Grube et al., 2018; Schwenk et al., 2017).

3.2. Yars^{E196K} mice display a perturbation in sensory neuron identity

We have previously revealed that lumbar, but not cervical DRG of CMT2D mice display fewer NF200$^+$ mechanoreceptors/proprioceptors, and a concomitant increase in the percentage of peripherin$^+$ nociceptors

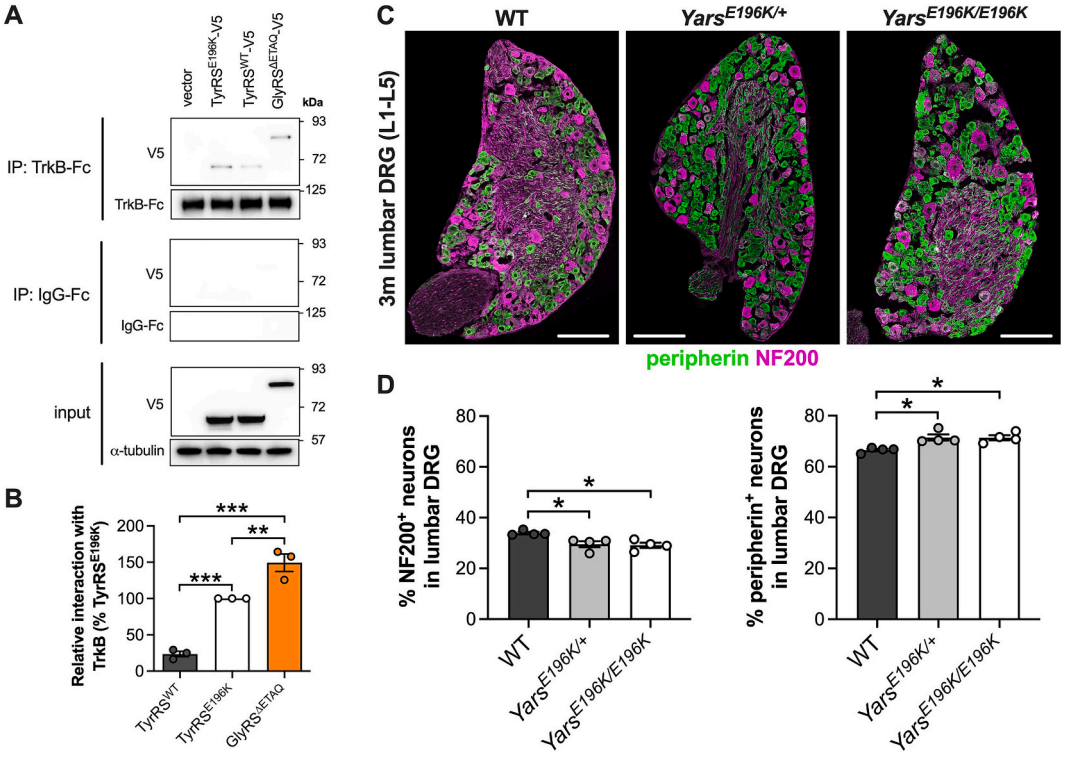

Fig. 1. TyrRS^{E196K} aberrantly interacts with the extracellular domain of TrkB underlying altered sensory neuron subtype proportions. (A) Representative western blots of *in vitro* pull-downs from NSC-34 cells showing that human TyrRS^{E196K} interacts with the extracellular domain of human TrkB-Fc to a greater extent than TyrRS^{WT}. GlyRS$^{\Delta ETAQ}$ was used as a positive control. *IP*, immunoprecipitation; *kDa*, kilodalton. (B) Quantification of the relative interactions between TyrRS^{WT}, TyrRS^{E196K} and GlyRS$^{\Delta ETAQ}$ with TrkB-Fc ($P < 0.001$ one-way ANOVA). $n = 3$. (C) Representative immunofluorescent images of 3 month-old wild-type, *Yars*$^{E196K/+}$ and *Yars*$^{E196K/E196K}$ lumbar DRG sections (10 μm) stained for NF200 (magenta) and peripherin (green). Scale bars = 100 μm. (D) *Yars*$^{E196K/+}$ and *Yars*$^{E196K/E196K}$ mice display a lower percentage of NF200$^+$ neurons (left graph, $P = 0.013$ Kruskal-Wallis test) and a higher percentage of peripherin$^+$ neurons (right graph, $P = 0.013$ Kruskal-Wallis test) in lumbar 1 (L1) to L5 DRG compared to wild-type. $n = 4$. For all graphs, $^*P < 0.05$, $^{**}P < 0.01$, $^{***}P < 0.001$ Šídák's/Dunn's multiple comparisons test; means ± standard error of the mean (SEM) plotted. See also Fig. S1. (For interpretation of the references to colour in this figure legend, the reader is referred to the web version of this article.)

(Sleigh et al., 2017a; Sleigh et al., 2020a). During pre-natal development, sensory neurons can express multiple Trk receptors, reaching their mature Trk identity and function after birth (Keeler et al., 2022). The neuropathic DRG phenotype is thus perhaps linked to the aberrant interaction between mutant GlyRS and the Trk receptors causing a subversion of sensory neuron differentiation.

Given that mutant TyrRS mis-associates with TrkB, we wanted to determine whether *Yars*^{E196K} mice display a similar alteration in sensory neuron populations. We therefore dissected lumbar DRG from 3 month-old wild-type, *Yars*$^{E196K/+}$ and *Yars*$^{E196K/E196K}$ mice and performed immunohistochemical analysis of NF200 and peripherin (Fig. 1C). Compared to wild-type littermate controls, we identified that both *Yars*$^{E196K/+}$ and *Yars*$^{E196K/E196K}$ mice display a lower percentage of NF200^{+} neurons and an increase in the percentage of peripherin^{+} neurons (Fig. 1D). Similar to mutant *Gars* mice, this phenotype was not present in *Yars*$^{E196K/+}$ cervical DRG (Fig. S1). Heterozygous and homozygous mutant *Yars* mice thus both phenocopy CMT2D mice in the spinal region-specific perturbation of sensory neuron identity.

To evaluate the severity of this sensory phenotype compared to the change observed in CMT2D models, the percentage of NF200^{+} neurons in lumbar DRG relative to wild-type (*n.b.*, not raw percentages) was calculated for *Yars*$^{E196K/+}$ (87.1 ± 3.5%) and *Yars*$^{E196K/E196K}$ (85.8 ± 3.0%), as well as 3 month-old *Gars*$^{\Delta ETAQ/+}$ mice (74.7 ± 1.3%; data not shown). All DRG assessments were performed by the same researcher (RLS), reducing variability, but relative values were required because the experiments were not performed or analysed in parallel. Statistical comparisons between the three ARS CMT genotypes indicate a difference (*$P = 0.020$ Kruskal-Wallis test), and that the reduction in NF200^{+} cells is greater in *Gars*$^{\Delta ETAQ/+}$ lumbar DRG than *Yars*$^{E196K/E196K}$ (*$P = 0.025$ Dunn's multiple comparisons test). Therefore, the severity of disruption in sensory neuron identity correlates with the extent of the mis-interaction between the mutant ARS protein and TrkB.

3.3. Body weight, NMJ innervation and grip strength are all unaffected in *Yars*^{E196K} mice at 3 months

The above DRG analyses, and all subsequent experiments, were performed in *Yars*^{E196K} mice on a C57BL/6 J background, which was chosen to allow for direct comparison with the CMT2D strains that are maintained on the same background in our laboratory. In the original assessment, when *Yars*^{E196K} mice were generated, experiments were performed at 2, 4 and 7 months of age and the mutation was maintained on a slightly different genetic background (C57BL/6 N) (Hines et al., 2022). In the study presented here, we chose to evaluate *Yars*^{E196K} mice at 3 and 9 months to extend the phenotyping age range and allow for evaluation of similarities with mutant *Gars* alleles, which we have extensively characterised at 3 months (Sleigh et al., 2017a; Sleigh et al., 2014c; Sleigh et al., 2020b; Sleigh et al., 2023).

First, we assessed the body weight of 3 month-old wild-type, *Yars*$^{E196K/+}$ and *Yars*$^{E196K/E196K}$ (Fig. S2). We observed no differences in body weight or relative body weight of females or males, corroborating previous analyses at 4 and 7 months (Hines et al., 2022). At 4 months, *Yars*$^{E196K/E196K}$ mice have reduced NCVs, thinner motor axons and impaired motor function and endurance, as assessed by the wire hang (inverted grid) test (Hines et al., 2022). We therefore analysed the architecture of NMJs and the maximum grip strength of *Yars*^{E196K} mice. We have previously identified a spectrum of vulnerability to degeneration of NMJs in different muscles in *Gars*$^{C201R/+}$ mice modelling CMT2D (Sleigh et al., 2014c; Sleigh et al., 2020b). At 3 months of age, the ETA muscle in the forearm is almost completely unaffected (≈4% denervation); in contrast, the hindlimb lumbricals and FDB muscles of the hindpaw display ≈43% and ≈63% denervated NMJs, respectively, whilst the forelimb lumbricals have an intermediate phenotype with ≈21% denervation. A similar pattern of vulnerability is also observed in *Gars*$^{\Delta ETAQ/+}$ mice at 3 months (data not shown).

These same four muscles were dissected from 3 month-old *Yars*^{E196K} mice and stained to assess NMJ architecture using combined antibodies against SV2/2H3 to identify motor neurons, and fluorescently labelled α-BTX to label post-synaptic AChRs (Fig. S3A). The extent of distal motor neuron pathology can be inferred by the degree of overlap between the pre- and post-synaptic staining and categorising NMJs as either fully innervated, partially denervated or vacant. We observed no NMJ denervation at 3 months of age in *Yars*$^{E196K/+}$ or *Yars*$^{E196K/E196K}$ mice in any of the four muscles (Fig. S3B). Moreover, the delay in NMJ maturation present in CMT2D mice, assessed by calculating the percentage of NMJs with multiple innervating motor neurons (*i.e.*, polyinnervation) (Sleigh et al., 2014c; Sleigh et al., 2020b), was also largely absent in *Yars*^{E196K} muscles (Fig. S3C). That is, except for a small, but significant, difference between forelimb lumbricals of heterozygous and homozygous mutants, which is likely a product of the lack of variability in the *Yars*$^{E196K/E196K}$ mouse sample, rather than being biologically meaningful.

Consistent with the lack of morphological disruption at the NMJ, we were unable to detect any difference in grip strength between wild-type and *Yars*^{E196K} genotypes in females or males (Fig. S4). This seemingly contrasts with previously performed wire hang assessments at 2 and 4 months in *Yars*$^{E196K/E196K}$ mice (Hines et al., 2022); however, the wire hang test measures muscle endurance whereas grip strength provides a readout of maximum strength.

3.4. *Yars*$^{E196K/E196K}$ motor neurons display reduced areas and increased ISR activation at 3 months

Motor neurons in the lumbar spinal cord of CMT2D mice are preserved, but display a reduction in area (Sleigh et al., 2023). To assess whether *Yars*^{E196K} mice have a similar phenotype, the L3-L5 spinal cord was sectioned and stained for ChAT to identify motor neurons in the anterior horns and p-eIF2α to assess ISR activation (Fig. 2A). We found that motor neuron numbers are similar between genotypes (Fig. 2B), while *Yars*^{E196K} homozygotes displayed a reduction in motor neuron area (Fig. 2C), similar to *Gars*$^{C201R/+}$ mice. As body weight is unaffected at this age, the reduction in cell area is independent from body size and is concordant with the smaller motor axon calibres identified in *Yars*$^{E196K/E196K}$ at 4 months (Hines et al., 2022). We also confirmed a clear increase in p-eIF2α staining within motor neurons of *Yars*$^{E196K/E196K}$ (Fig. 2D), replicating in the C57BL/6 J background previous results obtained in this neuropathy model (Hines et al., 2022).

3.5. In vivo axonal transport of signalling endosomes is unperturbed in *Yars*^{E196K} mice at 3 months

Gars$^{C201R/+}$ mice display impaired *in vivo* axonal transport of neurotrophin-containing signalling endosomes at 1 and 3 months of age, which manifests as a reduction in endosome trafficking speed after P15–16 (Sleigh et al., 2023). This defect was identified by injecting a fluorescent retrograde probe (H_CT) into the tibialis anterior and gastrocnemius muscles of anaesthetised mice, followed by time-lapse confocal imaging of the exposed sciatic nerve under terminal anaesthesia (Sleigh et al., 2020d). H_CT is internalised at the NMJ and then sorted into BDNF^{+} and TrkB^{+} signalling endosomes for retrograde axonal transport within motor axons (Bercsenyi et al., 2014). Individual endosomes can be imaged, tracked and their dynamic properties assessed.

We therefore used H_CT to identify whether *Yars*^{E196K} mice display an impairment in endosome axonal transport at 3 months of age (Fig. 3A). However, rather than injecting both the tibialis anterior and gastrocnemius muscles together, we performed assessments of transport separately in these two muscles, as we have recently determined that their innervating axons can be differentially affected by disease in a mouse model of amyotrophic lateral sclerosis (Tosolini et al., 2022). Importantly, the most common clinical signs reported in a small cohort of familial DI-CMTC patients were weakness and atrophy of the tibialis

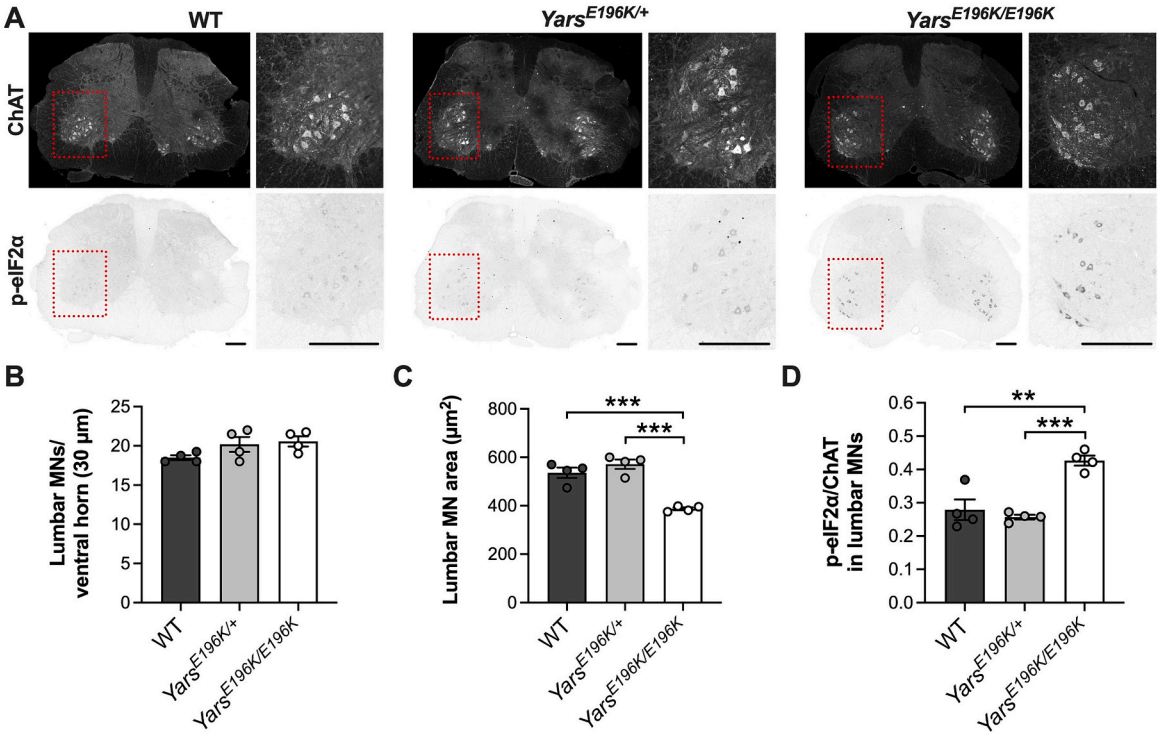

Fig. 2. Motor neurons of homozygous *Yars*^{E196K} mice have reduced area at 3 months. (A) Representative immunofluorescent images of 3 month-old wild-type, *Yars*$^{E196K/+}$ and *Yars*$^{E196K/E196K}$ lumbar spinal cord sections (30 µm) stained for ChAT (top) and p-eIF2α (bottom). The red dashed line boxes highlight the magnified regions shown to the right of each section. Scale bars = 200 µm. (B) *Yars*^{E196K} mice display no lumbar motor neuron (MN) loss ($P = 0.130$ one-way ANOVA). (C—D) Motor neurons from homozygous, but not heterozygous *Yars*^{E196K} mice display a smaller area than wild-type (C, $P < 0.001$ one-way ANOVA) and have increased levels of p-eIF2α (D, $P < 0.001$ one-way ANOVA), indicative of activation of the integrated stress response (ISR). For all graphs, $n = 4$; $^{**}P < 0.01$, $^{***}P < 0.001$ Šidák's multiple comparisons test; means ± SEM plotted. (For interpretation of the references to colour in this figure legend, the reader is referred to the web version of this article.)

anterior and gastrocnemius (Pan et al., 2020), thus these two muscles are clinically relevant in the disease. However, in motor neurons innervating the tibialis anterior muscle, we observed no differences between genotypes in signalling endosome speed (Fig. 3B-C), the percentage of time that endosomes remained stationary (Fig. 3D) or the percentage of endosomes that paused (Fig. 3E). A similar pattern was observed in gastrocnemius-innervating motor neurons (Fig. 3F-I). Together, these results indicate that at 3 months of age, *Yars*^{E196K} mice display no disruption in axonal transport of signalling endosomes, commensurate with the body weight, NMJ and grip strength analyses.

We have previously determined that signalling endosome trafficking impairment in CMT2D mice correlates with reduced availability in the sciatic nerve of motor adaptor proteins critical to endosome transport (Sleigh et al., 2023). As we see no transport deficits in the sciatic nerve of *Yars*^{E196K} mice at 3 months, we hypothesised that there would be no corresponding change in the levels of the adaptor proteins Snapin (Cai et al., 2010), Hook1 (Olenick et al., 2019) or RILP (Jordens et al., 2001), which have been shown to play a role in signalling endosome transport. We also assessed the levels of dynein intermediate chain (DIC), a major component of the retrograde motor protein cytoplasmic dynein, and probed for dynein intermediate chain phosphorylation at residue S81 (p-DIC), which facilitates the selective recruitment of the motor to signalling endosomes for retrograde trafficking upon Trk activation (Mitchell et al., 2012). Contrary to expectation, we saw that DIC phosphorylation was reduced in *Yars*$^{E196K/+}$ sciatic nerves, alongside an increase in RILP levels. In *Yars*$^{E196K/E196K}$ nerves, dimeric Snapin (dSnapin) levels were reduced, whereas p-DIC, Hook1 and RILP were all increased (Fig. 4). Although the cause of these changes is unknown, it is enticing to speculate that there may be compensatory mechanisms in endosome adaptor availability that ensure signalling endosome transport remains unaffected in mutant animals at 3 months of age.

Summarising the phenotype of *Yars*^{E196K} mice on a C57BL/6 J background at 3 months, we observed a perturbation in sensory neuron identity, reduced lumbar motor neuron cell body areas and changes in adaptor protein levels in the sciatic nerve, but no deficits in body weight, NMJ innervation, maximal grip strength or *in vivo* axonal transport of signalling endosomes.

3.6. *Yars*$^{E196K/E196K}$ mice display marginally reduced body weight, but normal motor innervation and function at 9 months

As we detected only subtle changes in *Yars*^{E196K} mice at 3 months of age, we decided to re-assess mice at 9 months of age. We observed a small reduction in body weight and relative body weight of 9 month-old *Yars*$^{E196K/E196K}$ females compared to *Yars*$^{E196K/+}$, but not wild-type mice of the same sex (Fig. S5A—B). Males were unaffected, suggesting that there may be a subtle sex-specific defect. When relative body weights of females and males were combined, we also saw a mild deficit in *Yars*$^{E196K/E196K}$ compared to *Yars*$^{E196K/+}$, but again not in comparison to wild-type animals (Fig. S5C).

Mirroring the lack of a large reduction in body weight, we observed no degeneration of NMJs across the same four muscles analysed at 3 months (Fig. S6). Of the six *Yars*$^{E196K/E196K}$ mice analysed, five were females, indicating that there is unlikely to be sex-specific denervation. This is supported by the finding that *Yars*^{E196K} females and males display normal grip strength at 9 months (Fig. S7). Again replicating the scenario at 3 months, we detected no lumbar motor neuron loss at 9 months and a similar reduction in cell body areas (Fig. 5).

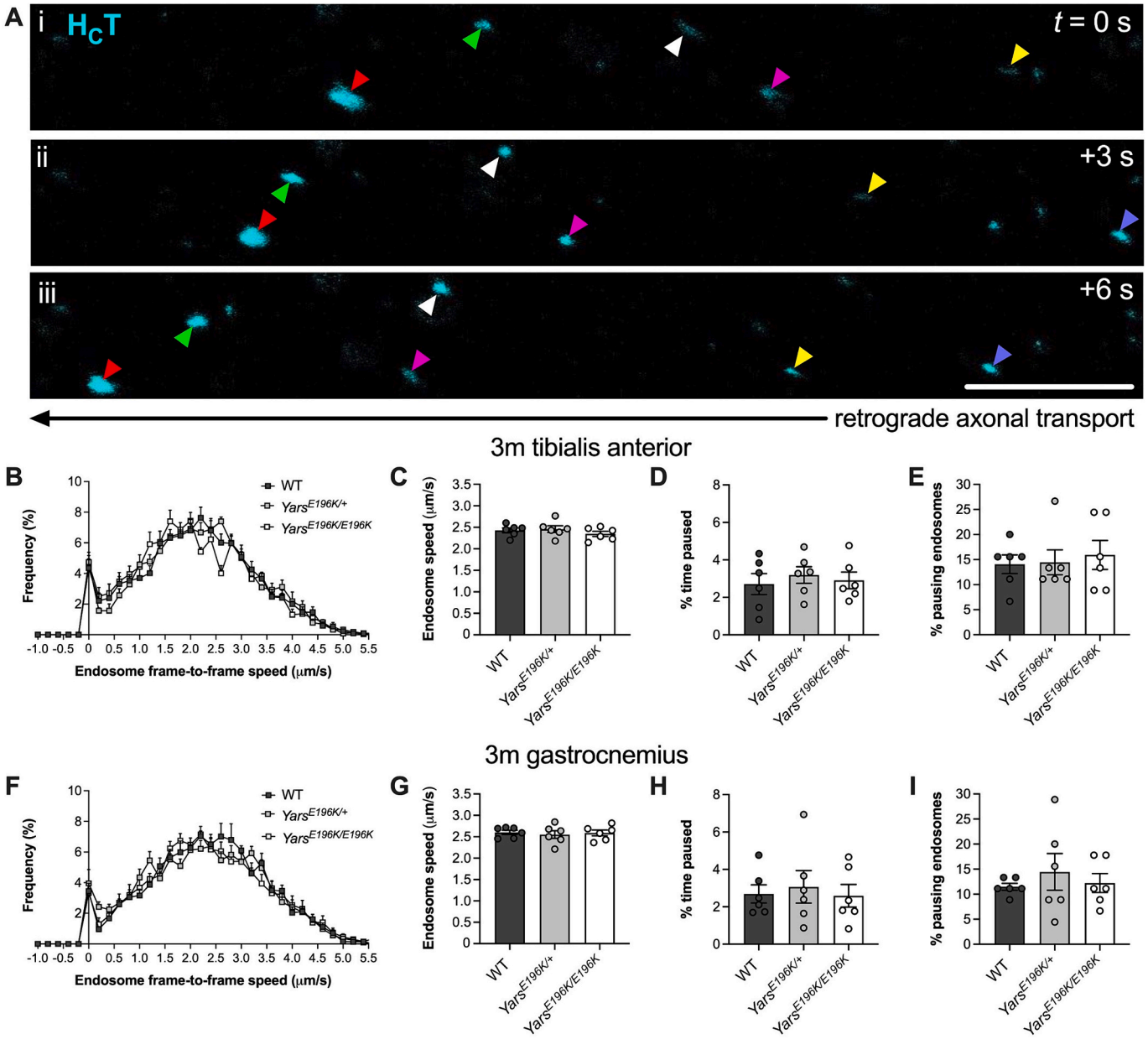

Fig. 3. *In vivo* axonal transport of signalling endosomes is unaffected in *Yars*^{E196K} mice at 3 months. (A) Representative time-lapse confocal images of signalling endosomes labelled with an atoxic fluorescent fragment of tetanus neurotoxin (H_CT, cyan) being retrogradely transported within peripheral nerve axons of live, anaesthetised mice. H_CT-positive endosomes are individually tracked to quantitatively assess their dynamics. Colour-coded arrowheads identify six different endosomes. Scale bar = 10 μm. (B) Frame-to-frame speed histogram of signalling endosomes being transported within motor neurons innervating the tibialis anterior muscle of wild-type, *Yars*$^{E196K/+}$ and *Yars*$^{E196K/E196K}$ mice aged 3 months. (C-E) There is no difference between genotypes in signalling endosome speed (C, $P = 0.487$), the percentage of time paused (D, $P = 0.781$) or the percentage of pausing endosomes (E, $P = 0.919$ Kruskal-Wallis test) in motor neurons innervating the tibialis anterior muscle. (F) Frame-to-frame speed histogram of signalling endosomes being transported within motor neurons innervating the gastrocnemius muscle of wild-type, *Yars*$^{E196K/+}$ and *Yars*$^{E196K/E196K}$ mice aged 3 months. (G-I) There is no difference between genotypes in signalling endosome speed (G, $P = 0.871$), the percentage of time paused (H, $P = 0.873$) or the percentage of pausing endosomes (I, $P = 0.671$) in motor neurons innervating the gastrocnemius muscle. Endosomes within tibialis anterior- and gastrocnemius-innervating axons were analysed in the same mice. For all graphs, genotypes were compared using one-way ANOVAs, unless otherwise stated; $n = 6$; means ± SEM plotted. See also Fig. S8. (For interpretation of the references to colour in this figure legend, the reader is referred to the web version of this article.)

3.7. In vivo endosome axonal transport is defective in Yars$^{E196K/E196K}$ *mice at 9 months*

We next evaluated *in vivo* axonal transport of signalling endosomes in motor axons innervating the tibialis anterior and gastrocnemius muscles of 9 month-old mice. *Yars*$^{E196K/+}$ mice were indistinguishable from wild-type (Fig. 6 and Fig. S8). However, *Yars*$^{E196K/E196K}$ mice displayed a reduction in endosome trafficking speeds in tibialis anterior-innervating neurons, coupled with an increase in the percentage of pausing endosomes (Fig. 6A-D and Fig. S8A-B). This deficit appears to be selective to neurons innervating the tibialis anterior, as we saw no such impairments in gastrocnemius-innervating neurons (Fig. 6E-H and Fig. S8C).

To assess whether the heterozygous mutants develop transport dysfunction with increased age, we assessed endosome dynamics at 15 months in both tibialis anterior- and gastrocnemius-innervating motor neurons in *Yars*$^{E196K/+}$ mice (Fig. S9). There was a small, but significant

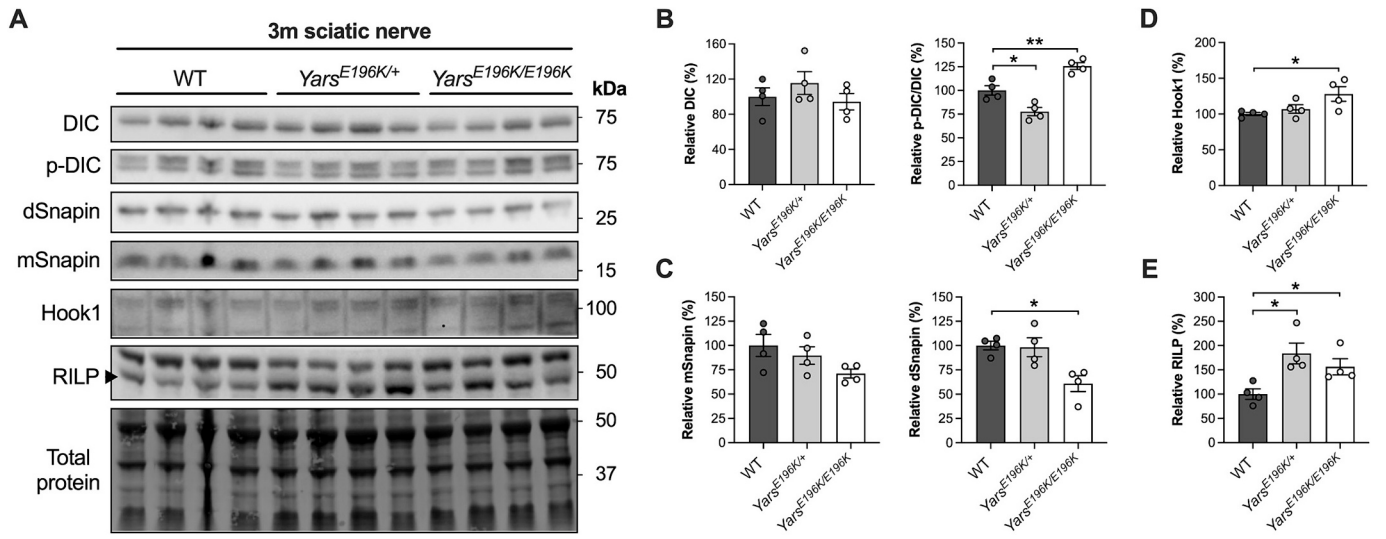

Fig. 4. Complementary changes in endosome adaptor levels are observed in *Yars*^{E196K} sciatic nerves at 3 months. (A) Western blots of dynein intermediate chain (DIC), phosphorylated DIC (p-DIC) and dynein adaptor proteins Snapin, Hook1 and RILP in sciatic nerves from 3 month-old wild-type, *Yars*$^{E196K/+}$ and *Yars*$^{E196K/E196K}$ mice. *kDa*, kilodalton. (B-E) Densitometric analyses of DIC (B, left, $P = 0.399$), p-DIC relative to DIC (B, right, $P < 0.001$), monomeric Snapin (mSnapin, C, left, $P = 0.113$), dimeric Snapin (dSnapin, C, right, $P < 0.01$), Hook1 (D, $P = 0.046$) and RILP (E, $P = 0.018$). The ratio of p-DIC to DIC is reduced in *Yars*$^{E196K/+}$ and increased in *Yars*$^{E196K/E196K}$, the level of dSnapin is reduced and Hook1 increased in *Yars*$^{E196K/E196K}$, and RILP is increased in both *Yars*^{E196K} genotypes. For all graphs, genotypes were compared using one-way ANOVAs; $n = 4$; $^{*}P < 0.05$, $^{**}P < 0.01$ Šídák's multiple comparisons test; means ± SEM plotted.

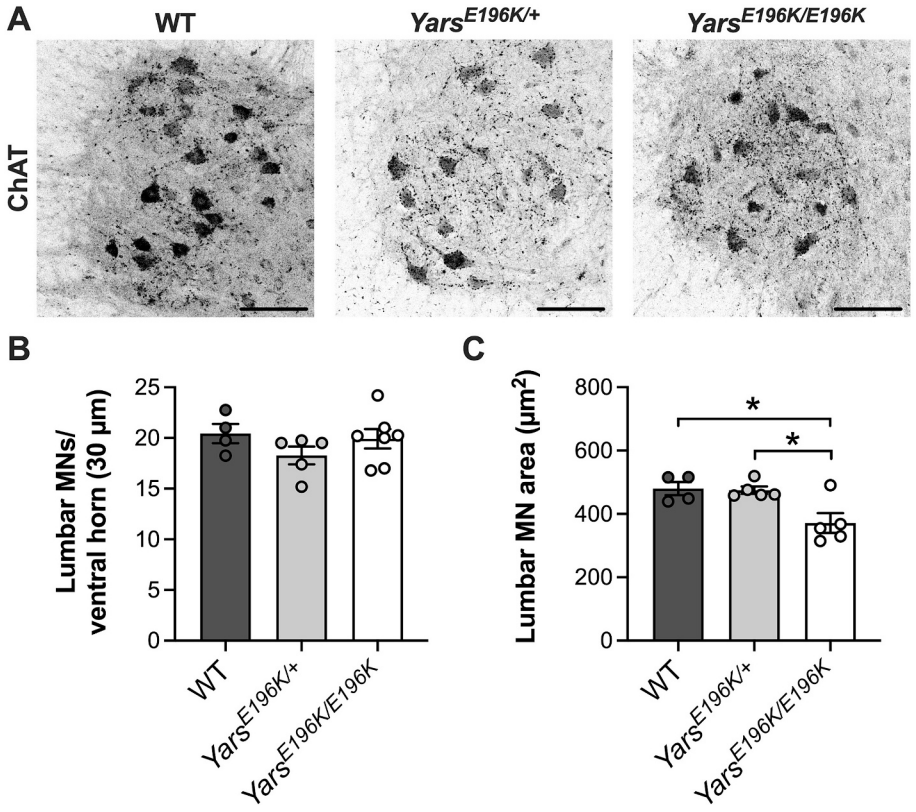

Fig. 5. Motor neuron cell body areas are reduced at 9 months in *Yars*^{E196K} homozygotes. (A) Representative immunofluorescent images of 9 month-old wild-type, *Yars*$^{E196K/+}$ and *Yars*$^{E196K/E196K}$ lumbar spinal cord sections (30 µm) stained for ChAT. Scale bars = 100 µm. (B) *Yars*^{E196K} mice display no lumbar motor neuron (MN) loss ($P = 0.320$ one-way ANOVA). $n = 4$–7. (C) Motor neurons from homozygous *Yars*^{E196K} mice exhibit smaller cell body areas than *Yars*$^{E196K/+}$ and wild-type mice (C, $P = 0.010$ one-way ANOVA). $^{*}P < 0.05$ Šídák's multiple comparisons test. $n = 4$–5. For both graphs, means ± SEM plotted.

increase in the percentage of time paused at 15 months compared with 9 months; however, there was no reduction in endosome speed or the percentage of pausing cargoes, indicating that axonal transport of signalling endosomes remains largely unaffected in aged *Yars*$^{E196K/+}$ mice.

We also evaluated endosome adaptor levels in 9 month-old sciatic nerves to determine whether any clear patterns could be linked to the transport disruption. None of the significant changes identified in 3 month-old nerves were replicated in the older mice and fewer changes

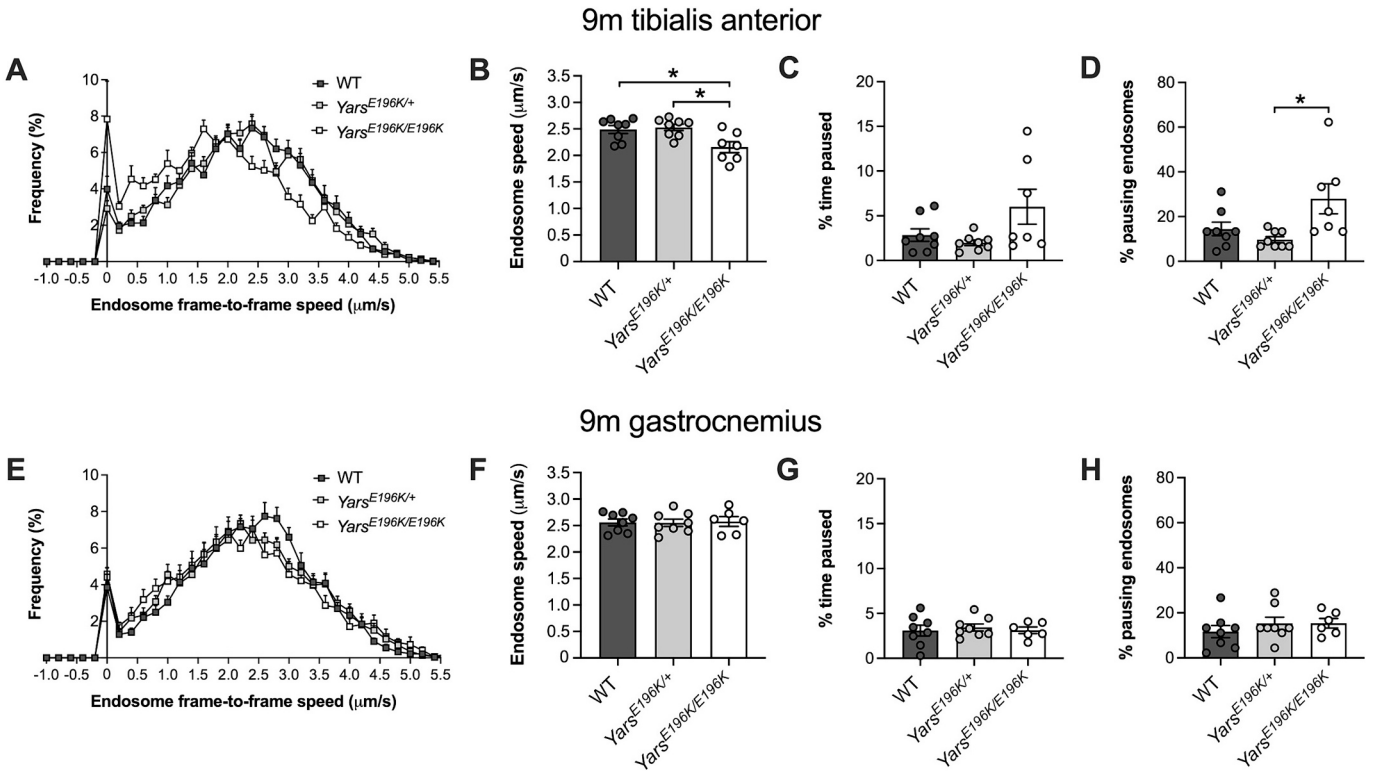

Fig. 6. *In vivo* axonal transport is selectively impaired in $Yars^{E196K}$ homozygotes at 9 months. (A) Frame-to-frame speed histogram of signalling endosomes being transported within motor neurons innervating the tibialis anterior muscle of wild-type, $Yars^{E196K/+}$ and $Yars^{E196K/E196K}$ mice aged 9 months. (B) Signalling endosome speed is reduced in tibialis anterior-innervating axons of $Yars^{E196K/E196K}$ mice ($P = 0.007$). (C—D) The percentage of time paused is unaffected (C, $P = 0.053$), but the percentage of pausing endosomes is increased (D, $P = 0.014$) in tibialis anterior-innervating axons of $Yars^{E196K/E196K}$ mice. (E) Frame-to-frame speed histogram of signalling endosomes being transported within motor neurons innervating the gastrocnemius muscle of wild-type, $Yars^{E196K/+}$ and $Yars^{E196K/E196K}$ mice aged 9 months. (F—H) There is no difference between genotypes in signalling endosome speed (F, $P = 0.971$), percentage of time paused (G, $P = 0.848$) or the percentage of pausing endosomes (H, $P = 0.529$ Kruskal-Wallis test) in motor neurons innervating the gastrocnemius. Endosomes within tibialis anterior- and gastrocnemius-innervating axons were analysed from the same mice. For all graphs, genotypes were compared using one-way ANOVAs, unless otherwise stated; $n = 6$–8; $^*P < 0.05$ Šidák's multiple comparisons test; means ± SEM plotted. See also Fig. S8 and Fig. S9.

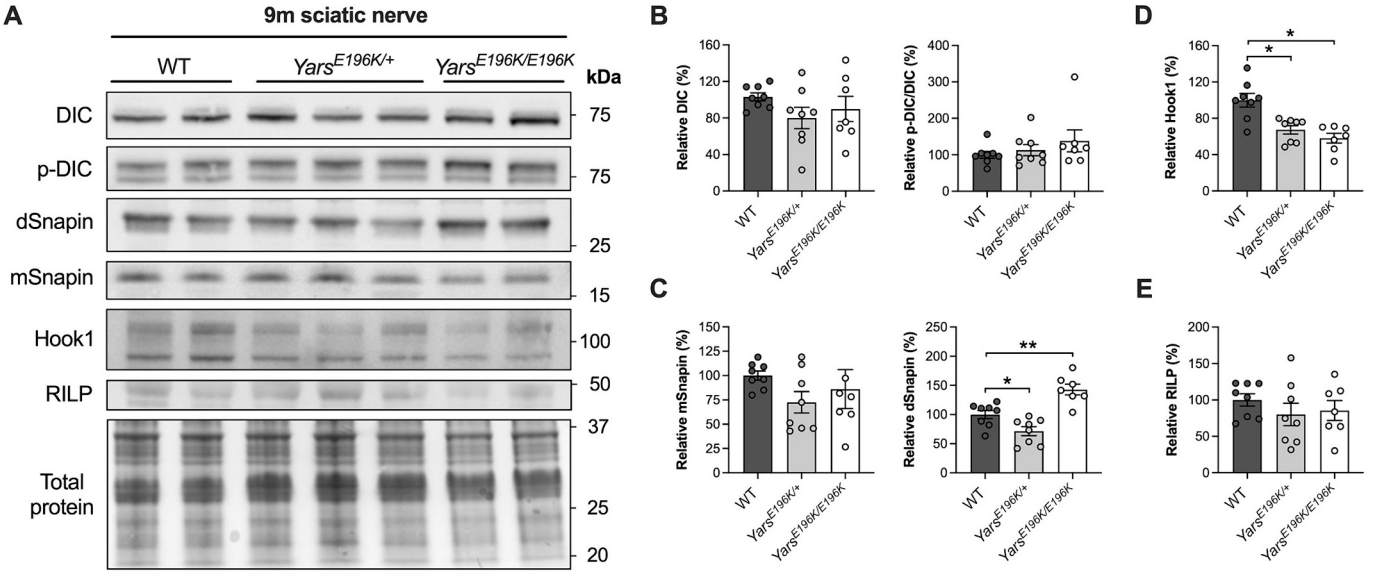

Fig. 7. Endosome adaptor levels are altered in 9 month-old $Yars^{E196K}$ sciatic nerves. (A) Western blots of dynein intermediate chain (DIC), phosphorylated DIC (p-DIC) and dynein adaptor proteins Snapin, Hook1 and RILP in sciatic nerves from 9 month-old wild-type, $Yars^{E196K/+}$ and $Yars^{E196K/E196K}$ mice. *kDa*, kilodalton. (B-E) Densitometric analyses of DIC (B, left, $P = 0.298$), p-DIC relative to DIC (B, right, $P = 0.541$ Kruskal-Wallis test), monomeric Snapin (mSnapin, C, left, $P = 0.320$), dimeric Snapin (dSnapin, C, right, $P < 0.001$), Hook1 (D, $P = 0.003$ Kruskal-Wallis test) and RILP (E, $P = 0.517$). The level of dSnapin is reduced in $Yars^{E196K/+}$ and increased in $Yars^{E196K/E196K}$, and the level of Hook1 is reduced in both $Yars^{E196K}$ genotypes. For all graphs, genotypes were compared using one-way ANOVAs, unless otherwise stated; $n = 7$–8; $^*P < 0.05$, $^{**}P < 0.01$ Šídák's/Dunn's multiple comparisons test; means ± SEM plotted.

were observed in homozygous mutants at the later time point (Fig. 7). At 9 months, *Yars*$^{E196K/+}$ mice displayed reduced expression of dSnapin and Hook1, whereas *Yars*$^{E196K/E196K}$ showed higher levels of dSnapin and lower levels of Hook1 (Fig. 7C-D).

3.8. Injection of TyrRS^{E196K} into wild-type muscle impairs endosome axonal transport

We have previously shown that injection of recombinant mutant GlyRS into wild-type muscles is sufficient to trigger non-cell autonomous impairment of endosome transport in otherwise healthy motor axons and that providing excess BDNF is able to overcome this disruption (Sleigh et al., 2023). As mutant TyrRS aberrantly associates with the ECD of TrkB, we hypothesised that this mis-interaction at the nerve-muscle interface may be impairing BDNF-TrkB signalling and thus driving the trafficking defect observed in *Yars*$^{E196K/E196K}$ mice. To test this idea, we bilaterally co-injected H_CT with TyrRS into the tibialis anterior muscles of wild-type mice, with one side receiving TyrRS^{WT} and the other TyrRS^{E196K} (Fig. 8). TyrRS^{WT} had no impact on signalling endosome axonal transport compared to vehicle-treated mice, whereas TyrRS^{E196K} caused a slow-down in endosome transport speeds compared to both vehicle and TyrRS^{WT} (Fig. 8A-B), without observable differences in pausing (Fig. 8C-D). These data indicate that DI-CMTC-causing mutant TyrRS within muscles is sufficient to non-cell autonomously impair signalling endosome axonal transport in wild-type mice.

To assess a possible relationship between the binding capacity of mutant ARS proteins and their effect on signalling endosome transport, we calculated the endosome transport speeds in wild-type mice receiving intramuscular injections of mutant GlyRS and mutant TyrRS relative to vehicle-treated controls (*n.b.*, not raw speeds). Injection of GlyRS^{L129P} and GlyRS^{G240R} caused endosomes to be transported at 75.5 ± 3.6% and 75.7 ± 3.4% of control, respectively (Sleigh et al., 2023), whereas TyrRS^{E196K} resulted in transport at 87.0 ± 3.1% of vehicle-injected mice. Mutant forms of GlyRS thus cause a greater impact on transport than TyrRS^{E196K} (*versus* GlyRS^{L129P} $P = 0.037$ and *versus* GlyRS^{G240R} $P = 0.038$, unpaired *t*-tests), meaning that the axonal transport disruption caused by mutant ARS proteins correlates with the extent of their aberrant interaction with the ECD of TrkB.

3.9. Augmenting BDNF levels in muscles of Yars$^{E196K/E196K}$ mice rescues axonal transport

Boosting BDNF, but not NT-3 or NT-4, in muscles of CMT2D mice corrects the impairment in signalling endosome axonal transport (Sleigh et al., 2023). As *Yars*$^{E196K/E196K}$ mice display a muscle-selective and age-dependent disruption in transport, similar in nature to that observed in CMT2D mice (Sleigh et al., 2023), we wished to establish whether increasing the availability of BDNF could also alleviate the trafficking disruption in this DI-CMTC model. To do so, we harnessed two different strategies – an acute paradigm with recombinant BDNF and a longer-term approach with AAV8-mediated, muscle-selective BDNF expression (Fig. 9A).

We first evaluated the short-term effect of injecting recombinant human mature BDNF into muscles of 9 month-old *Yars*$^{E196K/E196K}$ mice. This was done by co-injecting PBS vehicle control plus fluorescent H_CT into one tibialis anterior muscle, and BDNF together with H_CT into the contralateral muscle; signalling endosome transport was then sequentially assessed in both sciatic nerves 4–8 h-post injection. BDNF treatment caused an overt increase in the speed of signalling endosomes without significantly affecting pausing (Fig. 9B-E), indicating that intramuscular injection of this neurotrophin is capable of rescuing the trafficking deficit. The endosome transport dynamics of vehicle-treated mice were similar to those previously identified in tibialis anterior-innervating axons of 9 month-old *Yars*$^{E196K/E196K}$ mice (average speed: untreated 2.16 ± 0.1 μm/s *versus* vehicle-treated 2.24 ± 0.1 μm/s, $P = 0.615$ unpaired *t*-test).

The impact of longer-term exposure of *Yars*$^{E196K/E196K}$ muscles to increased BDNF availability was analysed by injecting 8 month-old mice with AAV8-tMCK-eGFP control into one tibialis anterior and AAV8-tMCK-BDNF into the contralateral muscle. We have previously confirmed that the combination of muscle-tropic AAV serotype 8 (Wang et al., 2005) with the muscle-specific promoter tMCK (Wang et al., 2008) drives a robust increase in BDNF expression in muscles up to at least 30 days *in vivo* (Sleigh et al., 2023). We therefore adapted this approach and treated 8 month-old *Yars*$^{E196K/E196K}$ mice with bilateral injections of AAV into tibialis anterior muscles, before assessing transport of signalling endosomes at 9 months. We first confirmed that AAV treatment did indeed drive transgene expression in tibialis anterior muscles (Fig. S10). We then showed that treatment with AAV8-tMCK-BDNF caused a strong increase in signalling endosome transport speed (Fig. 9F-G), without significantly altering pausing (Fig. 9H-I). Once again, we confirmed that the control virus had no impact on transport by comparing AAV8-tMCK-eGFP-treated mice with the original tibialis anterior-innervating axon data from 9 month-old *Yars*$^{E196K/E196K}$ mice shown in Fig. 6 (average speed: untreated 2.16 ± 0.1 μm/s *versus* eGFP-treated 2.06 ± 0.1 μm/s, $P = 0.562$ unpaired *t*-test). This indicates that treatment with AAV8-tMCK-BDNF has a local effect within the injected muscle and does not systemically affect transport.

Given the female-specific reduction in *Yars*$^{E196K/E196K}$ body weight (Fig. S5), we compared transport in tibialis anterior-innervating neurons between 9 month-old *Yars*$^{E196K/E196K}$ females and males, grouping all mice not receiving BDNF treatment (*i.e.*, incorporating PBS vehicle- and

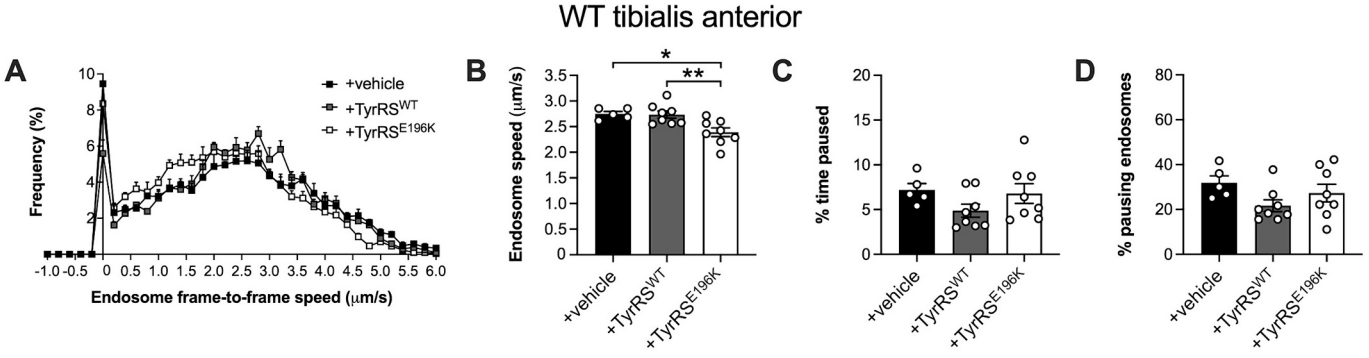

Fig. 8. Exposure of wild-type motor terminals to TyrRS^{E196K}, but not TyrRS^{WT}, impairs *in vivo* axonal transport. (A) Endosome frame-to-frame speed histograms of 2–4-month-old wild-type (WT) mice receiving either unilateral tibialis anterior injections of PBS or bilateral injections of recombinant human TyrRS^{WT} into one tibialis anterior and TyrRS^{E196K} into the contralateral tibialis anterior. (B—D) TyrRS^{E196K} causes a slowdown in signalling endosome speed in otherwise healthy motor neurons (B, $P = 0.004$) without impacting the percentage of time paused (C, $P = 0.193$) or the percentage of pausing endosomes (D, $P = 0.153$). For all graphs, genotypes were compared using one-way ANOVAs; $n = 5$–8; *$P < 0.05$, **$P < 0.01$ Šídák's multiple comparisons test; means ± SEM plotted.

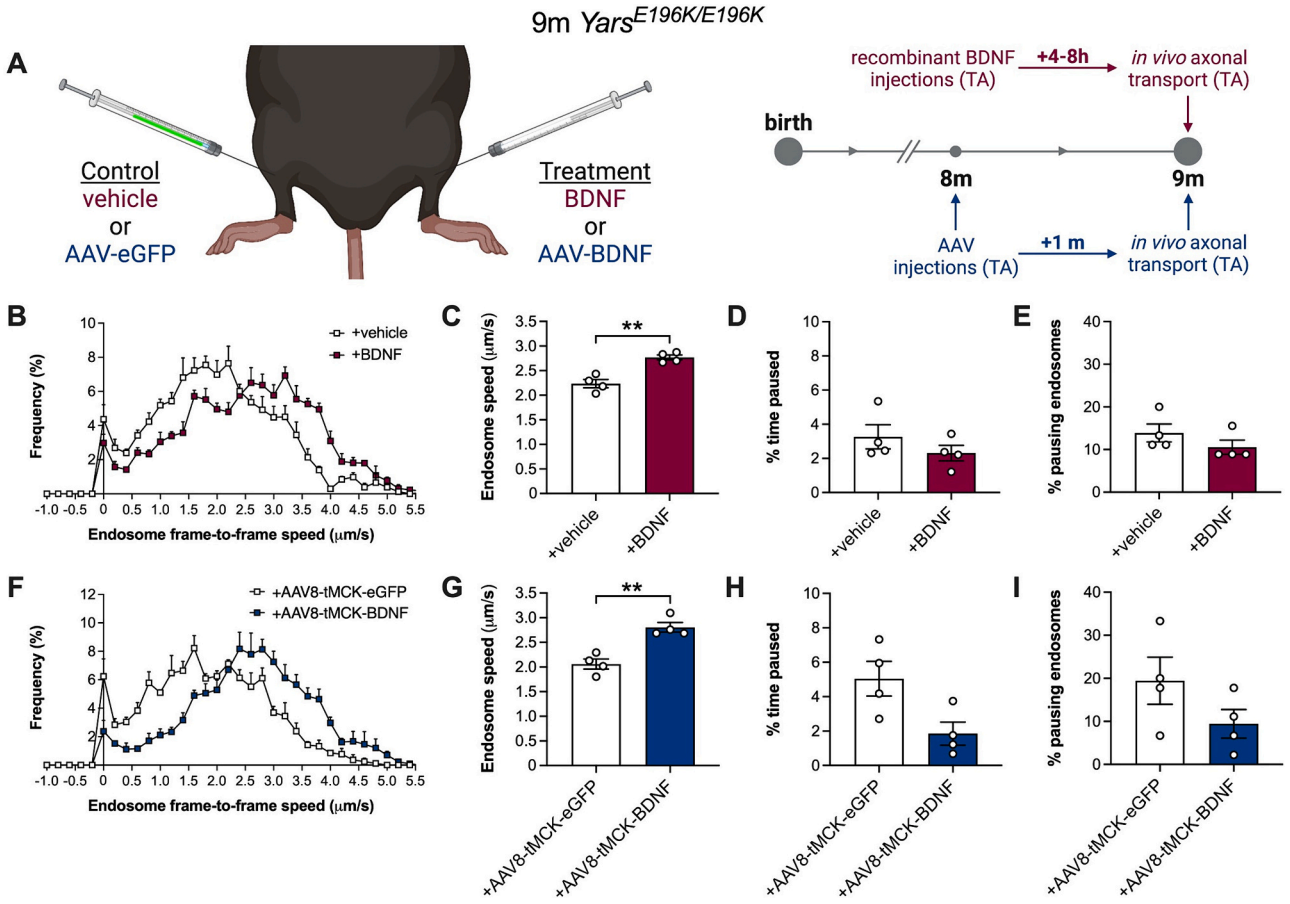

Fig. 9. Boosting BDNF in muscles of homozygous *Yars*^{E196K} mice rescues *in vivo* axonal transport. (A) Schematics depicting the dual-tibialis anterior (TA) injection paradigms (left) and timelines (right) used in experiments to assess the impact of BDNF treatment in *Yars*$^{E196K/E196K}$ mice. Animals either received dual injections of vehicle control *versus* recombinant BDNF at 9 months (maroon, top) or dual injections of AAV8-tMCK-eGFP *versus* AAV8-tMCK-BDNF at 8 months (blue, bottom). *In vivo* axonal transport of signalling endosomes was evaluated in tibialis anterior-innervating motor neurons at 9 months. (B) Frame-to-frame speed histogram of signalling endosomes being transported within motor neurons innervating the tibialis anterior muscle of 9 month-old *Yars*$^{E196K/E196K}$ mice 4–8 h post-treatment with intramuscular injections of vehicle or 25 ng recombinant BDNF. (C-E) BDNF increases the *in vivo* axonal transport speed of signalling endosomes in *Yars*$^{E196K/E196K}$ (C, $^{**}P = 0.004$), without impacting the percentage of time paused (D, $P = 0.324$) or the percentage of pausing endosomes (E, $P = 0.625$ Wilcoxon matched-pairs signed rank test). (F) Frame-to-frame speed histogram of signalling endosomes being transported within motor neurons innervating the tibialis anterior muscle of 9 month-old *Yars*$^{E196K/E196K}$ mice 29–30 days after bilateral injection of AAV8-tMCK-eGFP into one tibialis anterior and AAV8-tMCK-BDNF into the contralateral tibialis anterior. (G-I) AAV8-tMCK-BDNF increases signalling endosome speed in *Yars*$^{E196K/E196K}$ (G, $^{*}P = 0.032$), without impacting the percentage of time paused (H, $P = 0.116$) or the percentage of pausing endosomes (I, $P = 0.299$). For all graphs, treatments were compared using paired *t*-tests, unless otherwise stated; $n = 4$; means ± SEM plotted. See also Fig. S10 and Fig. S11. (For interpretation of the references to colour in this figure legend, the reader is referred to the web version of this article.)

AAV8-tMCK-eGFP-treated mice into the original 9 month data set). There was no difference in endosome trafficking between females and males (Fig. S11A-D), suggesting that sex-specific differences are restricted to body weight and that transport in both sexes is equally defective.

Finally, to better evaluate whether treatment with BDNF is able to impact endosome pausing, we combined control-treated and BDNF-treated data from the acute and long-term transport experiments. Doing so revealed that boosting intramuscular levels of BDNF has a clear rescue effect on the axonal transport disruption in DI-CMTC mice (Fig. S11E-H) – signalling endosome transport speeds were increased almost to wild-type levels, and both percentage of time paused and the percentage of pausing endosomes were reduced.

4. Discussion

Homozygous *Yars*^{E196K} mice have previously been validated as a useful model for DI-CMTC, showing reduced NCVs, diminished motor axon calibres and a decline in motor endurance (Hines et al., 2022). Here, we extend the temporal evaluation of *Yars*^{E196K} mice by assessing alternative features of peripheral nerve morphology and function at both 3 and 9 months. We identified several additional phenotypes pertinent to the human neuropathy, including distorted sensory neuron subpopulations, reduced motor neuron cell body areas, altered endosome adaptor levels within sciatic nerves, and impaired *in vivo* axonal transport of signalling endosomes (see Fig. S12 for a summary of the DI-CMTC phenotypes observed to date). This study provides the first evidence for axonal transport dysfunction in DI-CMTC and only the second study in which axonal transport has been identified as being impaired in mammalian peripheral neuropathy *in vivo*.

We also confirmed that motor neurons of *Yars*$^{E196K/E196K}$ mice on the C57BL/6 J background display a similar activation of the ISR as those mutants on C57BL/6 N (Spaulding et al., 2021), which indicates that the subtle change in genetic background is unlikely to have impacted the overall severity of these mice. This is important, because we did not observe reduction in NMJ innervation across four different muscles nor any decline in maximal grip strength; thus, previously reported deficits in wire hang endurance are unlikely to result from overt anatomical

changes at the neuromuscular synapse, but instead could reflect functional changes in synaptic physiology, similar to those identified in CMT2D mice (Spaulding et al., 2016). The decline in motor neuron area is concordant with the previously identified smaller calibres of motor axons, which likely contribute to the slower NCVs and reduced motor endurance without impacting NMJ innervation and maximum muscle force. Indeed, reduced NCV occurs without denervation in several mouse models of neuropathy (Baloh et al., 2009; Court et al., 2008; Morelli et al., 2017). Nonetheless, we might have overlooked subtle morphological alterations at the neuromuscular synapse (*e.g.*, reduced post-synaptic area or complexity), or by calculating the percentage of NMJs displaying degeneration, we might have missed denervated NMJs that have been rapidly lost from the muscle (Comley et al., 2022). Alternatively, NMJ pathology may be overt in other muscles (*e.g.*, the tibialis anterior).

The only clear phenotype that was present at 9 months, but not 3 months, was the axonal transport impairment, suggesting that the trafficking disruption in DI-CMTC is progressive, and therefore similar in nature to that identified in mutant *Gars* mice (Sleigh et al., 2023). Disturbances in axonal transport have been identified in models of many different forms of both genetic and acquired peripheral neuropathy (Beijer et al., 2019; Prior et al., 2017; Sleigh et al., 2019), including several different cellular and *in vivo* models of CMT2D (Benoy et al., 2018; Mo et al., 2018; Sleigh et al., 2023; Smith et al., 2022); however, whether these deficits are a primary cause of disease or simply a secondary consequence of neuropathology remains an open question. In the case of DI-CMTC, given the temporal profile of peripheral nerve phenotypes in our study and the Hines et al. manuscript (Hines et al., 2022), it would appear that the endosome trafficking deficits are a secondary feature of disease. Nevertheless, they represent a primary effect of mutant TyrRS and are likely to exacerbate pathology by reducing the long-range, pro-survival neurotrophin signalling from motor nerve terminals to the spinal cord. It remains to be determined at what stage the transport becomes impaired and whether assessments beyond 9 months will reveal additional phenotypes subsequent to the transport disruption, such as loss of NMJ integrity.

The relevance of changes in endosome motor adaptor protein levels in 3 and 9 month sciatic nerves of *Yars*^{E196K} mice remains unclear, as we did not see consistent patterns correlating with age and/or the development of axonal transport disruption. A possible explanation for this is that different motor adaptor proteins may be required for signalling endosome trafficking as they progress from distal to proximal segments of the axon (Cason and Holzbaur, 2022). Indeed, the retrograde delivery of signalling endosomes in motor neurons relies on Rab7 (Deinhardt et al., 2006), whereas different effectors mediate the retrograde transport and maturation of autophagic organelles (Cason et al., 2021). Therefore, impairments in BDNF-TrkB signalling at the axon terminal caused by mutant TyrRS interacting with TrkB may have multifarious age- and location-dependent effects on the endosome motor adaptors, obscuring a clear neuropathic signature. That being said, the three endosome adaptors that were increased at 3 months in *Yars*$^{E196K/E196K}$ nerves were no longer elevated at 9 months, perhaps indicative of a possible loss of compensatory mechanisms with age.

Replicating findings obtained with mutant GlyRS, we show that mutant TyrRS aberrantly associates with the ECD of the BDNF receptor TrkB and that injection of TyrRS^{E196K} into wild-type muscle is sufficient to impair *in vivo* axonal transport of signalling endosomes in otherwise healthy motor axons. We have previously determined that inhibition of BDNF-TrkB signalling in wild-type muscles, either pharmacologically or using BDNF blocking antibodies, results in impaired signalling endosome trafficking (Sleigh et al., 2023). Pharmacological inhibition of ERK1/2, which is a key pathway downstream of BDNF-TrkB, has a similar negative effect on axonal transport of signalling endosomes (Sleigh et al., 2023; Vargas et al., 2023). It is thus conceivable that TyrRS^{E196K} is mis-interacting with TrkB at motor nerve terminals, impinging upon BDNF signalling and ERK1/2 phosphorylation, thereby slowing down endosome trafficking. Consistent with this hypothesis, provision of excess BDNF in DI-CMTC muscles fully corrects the transport phenotype. As we did not detect deficits in this dynamic process in heterozygous *Yars*^{E196K} mice even at 15 months, it is likely to be a dose-dependent disruption. Consistent with this idea, mutant GlyRS, which shows a stronger association with the ECD of TrkB, causes a greater transport deficit when injected into wild-type mouse muscles, and CMT2D mice display an earlier and more severe trafficking defect.

The interaction between TyrRS^{E196K} and TrkB is likely to impair the ability of BDNF to signal through TrkB, which could result in the slowing of neurotrophin-containing signalling endosomes *via* several different, non-mutually exclusive mechanisms, including reduced transcription, translation, phosphorylation and/or recruitment of adaptor and motor proteins (Mitchell et al., 2012; Santos et al., 2010; Vargas et al., 2023; Villarin et al., 2016). We are currently working to understand the molecular mechanism underpinning the slowed transport and have previously discussed these possibilities (Sleigh et al., 2023), so will not elaborate further here. It remains unknown why the TyrRS^{E196K} dosage does not differentially affect the sensory neuron populations in lumbar DRG of *Yars*^{E196K} mice; however, the data suggest that, since this is a toxic gain-of-function, once a maximum threshold level of mutant TyrRS is available (such as that reached in the heterozygous mutants), no further changes to sensory neuron populations occur. In the future, it will be interesting to determine whether subtypes of NF200^{+} (*e.g.*, parvalbumin^{+} and parvalbumin^{-}) and peripherin^{+} (*e.g.*, CGRP^{+} and IB4^{+}) neurons are equally affected in DI-CMTC and if the cellular alterations drive changes in sensory behaviour, as has been shown in CMT2D mice (Sleigh et al., 2023).

Mutations in *YARS1* enhance the binding partners TRIM28 and HDAC1 (Bervoets et al., 2019), as well as F-actin (Ermanoska et al., 2023). In this study, TyrRS^{WT} also appears to interact with TrkB at a low level compared with mutant TyrRS, whereas previous data indicate that this is not the case for GlyRS^{WT} (Sleigh et al., 2017a; Sleigh et al., 2023). Therefore, it is possible that TyrRS^{WT} constitutively interacts with TrkB to exert a non-canonical function, rather than being a novel aberrant association, but further work is required to address this.

As aminoacyl-tRNA synthetases represent the largest protein family linked to CMT aetiology, it is an alluring prospect that they share a common pathomechanism, which can be targeted to treat the several different associated subtypes of CMTs. Supporting this possibility, mouse and fly models of CMT2D and DI-CMTC display protein synthesis impairments in motor neurons linked to the ISR, which are driven by tRNA^{Gly} sequestration and ribosome stalling in mutant *Gars* models (Niehues et al., 2015; Spaulding et al., 2021; Zuko et al., 2021). Moreover, co-genetic modifiers of pathology have been discovered in *Drosophila* models of *GARS1*- and *YARS1*-associated neuropathy (Ermanoska et al., 2014). Our work contributes another shared mechanism between CMT2D and DI-CMTC that causes impairment in signalling endosome axonal transport through perturbations of the BDNF-TrkB signalling axis. There is scope for this pathomechanism to be relevant to additional ARS-linked neuropathies, since structural relaxation and conformational opening have been reported for both CMT-linked alanyl-tRNA synthetase (Sun et al., 2021) and histidyl-tRNA synthetase (Blocquel et al., 2019) mutants. Mammalian models for other subtypes of ARS-linked neuropathy are not currently available to determine whether axonal transport disruption is impaired in a mammalian setting *in vivo*, although with the advent of CRISPR/Cas9 technology, they are likely forthcoming. While the interruption in cargo trafficking within axons may not be the primary cause of neuropathy linked to ARS mutations, it will certainly contribute to the demise of peripheral nerves and is a promising candidate process for pharmacological targeting (Gibbs et al., 2015; Guo et al., 2020).

Through acute and month-long treatment paradigms, we have shown that boosting the availability of BDNF at motor nerve terminals of *Yars*$^{E196K/E196K}$ mice rescues deficits in axonal transport of neurotrophin-containing signalling endosomes *in vivo*, replicating

findings in CMT2D mice (Sleigh et al., 2023). Targeting muscle may therefore provide an effective approach to treating ARS-linked neuropathies, although care must be taken with concentration, timing and duration of neurotrophic factor delivery to ensure the best chance of treatment success (Eggers et al., 2020). In combination with additional interventions that have proven beneficial in mutant *Gars* mice, including HDAC6 inhibition (Benoy et al., 2018; Mo et al., 2018; Smith et al., 2022), delivery of neurotrophin 3 (Ozes et al., 2021) and $VEGF_{165}$ (He et al., 2015), and provision of excess $tRNA^{Gly}$ (Zuko et al., 2021), boosting BDNF in muscles may serve as part of a combinatorial treatment to address the therapeutic needs of one of the most common inherited neuromuscular conditions.

Ethics approval and consent to participate

Experiments involving mice were performed under license from the UK Home Office in accordance with the Animals (Scientific Procedures) Act (1986) and were approved by the UCL Queen Square Institute of Neurology Ethical Review Committee.

Consent for publication

Not applicable.

Funding

This project was funded by the Medical Research Council [grant numbers MR/S006990/1, MR/Y010949/1 to JNS]; the Rosetrees Trust [grant number M806 to JNS, GS]; the UCL Neurogenetic Therapies Programme funded by The Sigrid Rausing Trust [to JNS, GS]; the UCL Therapeutic Acceleration Support scheme supported by funding from MRC IAA 2021 UCL MR/X502984/1 [to JNS]; the Human Frontier Science Program Long-Term Fellowship [grant number LT000220/2017-L to SS]; the National Institutes of Health [grant numbers R37 NS05415 to RWB, R35 GM139627 to XLY]; the Wellcome Trust [grant numbers 107116/Z/15/Z, 223022/Z/21/Z to GS]; and the UK Dementia Research Institute award [grant number UK DRI-1005] through UK DRI Ltd., principally funded by the UK Medical Research Council [to GS].

Materials & correspondence

AAV expression plasmids are covered by an MTA with OXGENE (UK). Material requests should be addressed to the corresponding author.

CRediT authorship contribution statement

Elena R. Rhymes: Investigation. **Rebecca L. Simkin:** Investigation. **Ji Qu:** Investigation. **David Villarroel-Campos:** Investigation. **Sunaina Surana:** Investigation. **Yao Tong:** Investigation. **Ryan Shapiro:** Investigation. **Robert W. Burgess:** Resources, Funding acquisition. **Xiang-Lei Yang:** Supervision, Funding acquisition. **Giampietro Schiavo:** Supervision, Funding acquisition. **James N. Sleigh:** Supervision, Investigation, Funding acquisition, Conceptualization.

Declaration of competing interest

The technology described in this work has been protected in the patent GB2303495.2 (patent applicant, UCL Business Ltd., status pending), in which GS and JNS are named as inventors. The other authors declare no competing interests.

Data availability

The data that support the findings of this study are available from the corresponding author, [JNS], upon reasonable request.

Acknowledgements

We thank Timothy J. Hines (Jackson Laboratory) for sharing the sequences of $Yars^{E196K}$ genotyping primers, K. Kevin Pfister (University of Virginia) for donating the p-DIC (S81) antibody, and personnel of the Denny Brown Laboratory (UCL) for assistance with mouse colonies. Fig. 9A, Fig. S12A and the graphical abstract were created using https://www.biorender.com.

Appendix A. Supplementary data

Supplementary data to this article can be found online at https://doi.org/10.1016/j.nbd.2024.106501.

References

Baloh, R.H., et al., 2009. Congenital hypomyelinating neuropathy with lethal conduction failure in mice carrying the *Egr2* I268N mutation. J. Neurosci. 29, 2312–2321.
Beijer, D., et al., 2019. Defects in axonal transport in inherited neuropathies. J. Neuromuscul. Dis. 6, 401–419.
Benoy, V., et al., 2018. HDAC6 is a therapeutic target in mutant *GARS*-induced Charcot-Marie-tooth disease. Brain 141, 673–687.
Berciano, J., et al., 2017. Intermediate Charcot-Marie-tooth disease: an electrophysiological reappraisal and systematic review. J. Neurol. 264, 1655–1677.
Bercsenyi, K., et al., 2014. Tetanus toxin entry. Nidogens are therapeutic targets for the prevention of tetanus. Science 346, 1118–1123.
Bervoets, S., et al., 2019. Transcriptional dysregulation by a nucleus-localized aminoacyl-tRNA synthetase associated with Charcot-Marie-tooth neuropathy. Nat. Commun. 10, 5045.
Blocquel, D., et al., 2017. Alternative stable conformation capable of protein misinteraction links tRNA synthetase to peripheral neuropathy. Nucleic Acids Res. 45, 8091–8104.
Blocquel, D., et al., 2019. CMT disease severity correlates with mutation-induced open conformation of histidyl-tRNA synthetase, not aminoacylation loss, in patient cells. Proc. Natl. Acad. Sci. USA 116, 19440–19448.
Cai, Q., et al., 2010. Snapin-regulated late endosomal transport is critical for efficient autophagy-lysosomal function in neurons. Neuron 68, 73–86.
Cason, S.E., Holzbaur, E.L.F., 2022. Selective motor activation in organelle transport along axons. Nat. Rev. Mol. Cell Biol. 23, 699–714.
Cason, S.E., et al., 2021. Sequential dynein effectors regulate axonal autophagosome motility in a maturation-dependent pathway. J. Cell Biol. 220, e202010179.
Chao, M.V., 2003. Neurotrophins and their receptors: a convergence point for many signalling pathways. Nat. Rev. Neurosci. 4, 299–309.
Comley, L.H., et al., 2022. Motor unit recovery following Smn restoration in mouse models of spinal muscular atrophy. Hum. Mol. Genet. 31, 3107–3119.
Court, F.A., et al., 2008. Remodeling of motor nerve terminals in demyelinating axons of periaxin-null mice. Glia 56, 471–479.
Deinhardt, K., et al., 2006. Rab5 and Rab7 control endocytic sorting along the axonal retrograde transport pathway. Neuron 52, 293–305.
Eggers, R., et al., 2020. GDNF gene therapy to repair the injured peripheral nerve. Front. Bioeng. Biotechnol. 8, 583184.
Ermanoska, B., et al., 2014. CMT-associated mutations in glycyl- and tyrosyl-tRNA synthetases exhibit similar pattern of toxicity and share common genetic modifiers in Drosophila. Neurobiol. Dis. 68, 180–189.
Ermanoska, B., et al., 2023. Tyrosyl-tRNA synthetase has a noncanonical function in actin bundling. Nat. Commun. 14, 999.
Froelich, C.A., First, E.A., 2011. Dominant intermediate Charcot-Marie-tooth disorder is not due to a catalytic defect in tyrosyl-tRNA synthetase. Biochemistry 50, 7132–7145.
Gibbs, K.L., et al., 2015. Regulation of axonal transport by protein kinases. Trends Biochem. Sci. 40, 597–610.
Gibbs, K.L., et al., 2016. *In vivo* imaging of axonal transport in murine motor and sensory neurons. J. Neurosci. Methods 257, 26–33.
Grice, S.J., et al., 2015. Dominant, toxic gain-of-function mutations in *gars* lead to non-cell autonomous neuropathology. Hum. Mol. Genet. 24, 4397–4406.
Grice, S.J., et al., 2018. Plexin-semaphorin signaling modifies neuromuscular defects in a drosophila model of peripheral neuropathy. Front. Mol. Neurosci. 11, 55.
Grube, L., et al., 2018. Mining the cecretome of C2C12 muscle cells: data dependent experimental approach to analyze protein secretion using label-free quantification and peptide based analysis. J. Proteome Res. 17, 879–890.
Guo, W., et al., 2020. Axonal transport defects and neurodegeneration: molecular mechanisms and therapeutic implications. Semin. Cell Dev. Biol. 99, 133–150.
He, W., et al., 2011. Dispersed disease-causing neomorphic mutations on a single protein promote the same localized conformational opening. Proc. Natl. Acad. Sci. USA 108, 12307–12312.
He, W., et al., 2015. CMT2D neuropathy is linked to the neomorphic binding activity of glycyl-tRNA synthetase. Nature 526, 710–714.
Hines, T.J., et al., 2022. Precision mouse models of *Yars*/dominant intermediate Charcot-Marie-tooth disease type C and *Sptlc1*/hereditary sensory and autonomic neuropathy type 1. J. Anat. 241, 1169–1185.

Jordanova, A., et al., 2006. Disrupted function and axonal distribution of mutant tyrosyl-tRNA synthetase in dominant intermediate Charcot-Marie-tooth neuropathy. Nat. Genet. 38, 197–202.
Jordens, I., et al., 2001. The Rab7 effector protein RILP controls lysosomal transport by inducing the recruitment of dynein-dynactin motors. Curr. Biol. 11, 1680–1685.
Keeler, A.B., et al., 2022. A developmental atlas of somatosensory diversification and maturation in the dorsal root ganglia by single-cell mass cytometry. Nat. Neurosci. 25, 1543–1558.
Mitchell, D.J., et al., 2012. Trk activation of the ERK1/2 kinase pathway stimulates intermediate chain phosphorylation and recruits cytoplasmic dynein to signaling endosomes for retrograde axonal transport. J. Neurosci. 32, 15495–15510.
Mo, Z., et al., 2018. Aberrant GlyRS-HDAC6 interaction linked to axonal transport deficits in Charcot-Marie-tooth neuropathy. Nat. Commun. 9, 1007.
Morelli, K.H., et al., 2017. Severity of demyelinating and axonal neuropathy mouse models is modified by genes affecting structure and function of peripheral nodes. Cell Rep. 18, 3178–3191.
Morelli, K.H., et al., 2019. Allele-specific RNA interference prevents neuropathy in Charcot-Marie-tooth disease type 2D mouse models. J. Clin. Invest. 129, 5568–5583.
Niehues, S., et al., 2015. Impaired protein translation in *Drosophila* models for Charcot-Marie-tooth neuropathy caused by mutant tRNA synthetases. Nat. Commun. 6, 7520.
Nowaczyk, M.J., et al., 2017. A novel multisystem disease associated with recessive mutations in the tyrosyl-tRNA synthetase (*YARS*) gene. Am. J. Med. Genet. A 173, 126–134.
Olenick, M.A., et al., 2019. Dynein activator Hook1 is required for trafficking of BDNF-signaling endosomes in neurons. J. Cell Biol. 218, 220–233.
Oprescu, S.N., et al., 2017. Predicting the pathogenicity of aminoacyl-tRNA synthetase mutations. Methods 113, 139–151.
Ozes, B., et al., 2021. AAV1.NT-3 gene therapy in a CMT2D model: phenotypic improvements in $Gars^{P278KY/+}$ mice. Brain Commun. 3, fcab252.
Pan, Y., et al., 2020. Longitudinal 16-year study of dominant intermediate CMT type C neuropathy. Muscle Nerve 61, 111–115.
Pipis, M., et al., 2019. Next-generation sequencing in Charcot-Marie-tooth disease: opportunities and challenges. Nat. Rev. Neurol. 15, 644–656.
Prior, R., et al., 2017. Defective axonal transport: a common pathological mechanism in inherited and acquired peripheral neuropathies. Neurobiol. Dis. 105, 300–320.
Reilly, M.M., et al., 2011. Charcot-Marie-tooth disease. J. Peripher. Nerv. Syst. 16, 1–14.
Restani, L., et al., 2012. Botulinum neurotoxins a and E undergo retrograde axonal transport in primary motor neurons. PLoS Pathog. 8, e1003087.
Rossor, A.M., et al., 2013. Clinical implications of genetic advances in Charcot-Marie-tooth disease. Nat. Rev. Neurol. 9, 562–571.
Santos, A.R., et al., 2010. Regulation of local translation at the synapse by BDNF. Prog. Neurobiol. 92, 505–516.
Schorling, E., et al., 2019. Cost of illness in Charcot-Marie-tooth neuropathy: results from Germany. Neurology 92, e2027–e2037.
Schwenk, J.M., et al., 2017. The human plasma proteome draft of 2017: building on the human plasma PeptideAtlas from mass spectrometry and complementary assays. J. Proteome Res. 16, 4299–4310.
Seburn, K.L., et al., 2006. An active dominant mutation of glycyl-tRNA synthetase causes neuropathy in a Charcot-Marie-tooth 2D mouse model. Neuron 51, 715–726.
Sleigh, J.N., et al., 2014a. Chondrolectin affects cell survival and neuronal outgrowth in *in vitro* and *in vivo* models of spinal muscular atrophy. Hum. Mol. Genet. 23, 855–869.
Sleigh, J.N., et al., 2014b. Morphological analysis of neuromuscular junction development and degeneration in rodent lumbrical muscles. J. Neurosci. Methods 227, 159–165.
Sleigh, J.N., et al., 2014c. Neuromuscular junction maturation defects precede impaired lower motor neuron connectivity in Charcot-Marie-tooth type 2D mice. Hum. Mol. Genet. 23, 2639–2650.
Sleigh, J.N., et al., 2017a. Trk receptor signaling and sensory neuron fate are perturbed in human neuropathy caused by *gars* mutations. Proc. Natl. Acad. Sci. USA 114, E3324–E3333.
Sleigh, J.N., et al., 2017b. Neuropilin 1 sequestration by neuropathogenic mutant glycyl-tRNA synthetase is permissive to vascular homeostasis. Sci. Rep. 7, 9216.
Sleigh, J.N., et al., 2019. Axonal transport and neurological disease. Nat. Rev. Neurol. 15, 691–703.
Sleigh, J.N., et al., 2020a. Altered sensory neuron development in CMT2D mice is site-specific and linked to increased GlyRS levels. Front. Cell. Neurosci. 14, 232.
Sleigh, J.N., et al., 2020b. Developmental demands contribute to early neuromuscular degeneration in CMT2D mice. Cell Death Dis. 11, 564.
Sleigh, J.N., et al., 2020c. Mice carrying ALS mutant TDP-43, but not mutant FUS, display *in vivo* defects in axonal transport of signaling endosomes. Cell Rep. 30, 3655–3662.
Sleigh, J.N., et al., 2020d. *In vivo* imaging of anterograde and retrograde axonal transport in rodent peripheral nerves. Methods Mol. Biol. 2143, 271–292.
Sleigh, J.N., et al., 2020e. A video protocol for rapid dissection of mouse dorsal root ganglia from defined spinal levels. BMC. Res. Notes 13, 302.
Sleigh, J.N., et al., 2023. Boosting peripheral BDNF rescues impaired in vivo axonal transport in CMT2D mice. JCI Insight 8, e157191.
Smith, A.S.T., et al., 2022. HDAC6 inhibition corrects electrophysiological and axonal transport deficits in a human stem cell-based model of Charcot-Marie-tooth disease (type 2D). Adv. Biol. 6, e2101308.
Spaulding, E.L., et al., 2016. Synaptic deficits at neuromuscular junctions in two mouse models of Charcot-Marie-tooth type 2d. J. Neurosci. 36, 3254–3267.
Spaulding, E.L., et al., 2021. The integrated stress response contributes to tRNA synthetase-associated peripheral neuropathy. Science 373, 1156–1161.
Sun, L., et al., 2021. CMT2N-causing aminoacylation domain mutants enable Nrp1 interaction with AlaRS. Proc. Natl. Acad. Sci. USA 118, e2012898118.
Thomas, F.P., et al., 2016. Clinical, neurophysiological and morphological study of dominant intermediate Charcot-Marie-tooth type C neuropathy. J. Neurol. 263, 467–476.
Tinevez, J.Y., et al., 2017. TrackMate: an open and extensible platform for single-particle tracking. Methods 115, 80–90.
Tosolini, A.P., et al., 2021. Expanding the toolkit for *in vivo* imaging of axonal transport. J. Vis. Exp. 178, e63471.
Tosolini, A.P., et al., 2022. BDNF-dependent modulation of axonal transport is selectively impaired in ALS. Acta Neuropathol. Commun. 10, 121.
Tracewska-Siemiatkowska, A., et al., 2017. An expanded multi-organ disease phenotype associated with mutations in *YARS*. Genes 8, 381.
Vargas, J.N.S., et al., 2023. BDNF controls phosphorylation and transcriptional networks governing cytoskeleton organization and axonal regeneration. bioRxiv. https://doi.org/10.1101/2023.11.06.565775.
Villarin, J.M., et al., 2016. Local synthesis of dynein cofactors matches retrograde transport to acutely changing demands. Nat. Commun. 7, 13865.
Villarroel-Campos, D., et al., 2022. Dissection, *in vivo* imaging and analysis of the mouse epitrochleoanconeus muscle. J. Anat. 241, 1108–1119.
Wang, Z., et al., 2005. Adeno-associated virus serotype 8 efficiently delivers genes to muscle and heart. Nat. Biotechnol. 23, 321–328.
Wang, B., et al., 2008. Construction and analysis of compact muscle-specific promoters for AAV vectors. Gene Ther. 15, 1489–1499.
Wei, N., et al., 2019. Neurodegenerative Charcot-Marie-tooth disease as a case study to decipher novel functions of aminoacyl-tRNA synthetases. J. Biol. Chem. 294, 5321–5339.
Zhang, H., et al., 2021. Aminoacyl-tRNA synthetases in Charcot-Marie-tooth disease: a gain or a loss? J. Neurochem. 157, 351–369.
Zuko, A., et al., 2021. tRNA overexpression rescues peripheral neuropathy caused by mutations in tRNA synthetase. Science 373, 1161–1166.